TiO 2 /Cu 2 O/CuO Multi-Nanolayers as Sensors for H 2 and VOCs: An Experimental and Theoretical Investigation

Oleg Lupan, David Santos-Carballal, Nicolai Ababii, Nicolae Magariu, Sandra Hansen, Alexander Vahl, Lukas Zimoch, Mathias Hoppe, Thierry Pauporté, Vardan Galstyan, et al.

Cite this paper as : O. Lupan, D. Santos-Carballal, N. Ababii, N. Magariu, S. Hansen, A. Vahl, L. Zimoch, M. Hoppe, T. Pauporté, V. Galstyan, V. Sontea, L. Chow, N. H de Leeuw, F. Faupel, R. Adelung, E. Comini, $TiO_2/Cu_2O/CuO$ Multi-nanolayers as Sensors for H_2 and VOCs: An Experimental and Theoretical Investigation.
ACS Appl. Mater. Interfaces 13 (2021) 32363–32380.

$TiO_2/Cu_2O/CuO$ Multi-Nanolayers as Sensors for H_2 and VOCs: An Experimental and Theoretical Investigation

Oleg Lupan,[1,2,3,†] David Santos-Carballal,[4] Nicolai Ababii,[2] Nicolae Magariu,[2] Sandra Hansen,[1,†]

Alexander Vahl,[5] Lukas Zimoch,[1] Mathias Hoppe,[1] Thierry Pauporte,[6] Vardan Galstyan,[7]

Victor Sontea,[8,9] Lee Chow,[3] Franz Faupel,[5,†] Rainer Adelung,[1,†] Nora H de Leeuw,[4,10]

Elisabetta Comini[7]

[1] *Functional Nanomaterials, Faculty of Engineering, Institute for Materials Science, Kiel University, Kaiserstr. 2, D-24143, Kiel, Germany*
[2] *Center for Nanotechnology and Nanosensors, Technical University of Moldova, 168 Stefan cel Mare Av., MD-2004 Chisinau, Republic of Moldova*
[3] *Department of Physics, University of Central Florida, Orlando, FL 32816-2385, USA*
[4] *School of Chemistry, University of Leeds, Leeds LS2 9JT, United Kingdom*
[5] *Faculty of Engineering, Chair for Multicomponent Materials, Christian-Albrechts Universität zu Kiel, str. Kaiserstraße nr. 2, D-24143, 16 Kiel, Germany*
[6] *Institut de Recherche de Chimie Paris-IRCP, Chimie ParisTech, PSL Université, rue Pierre et Marie Curie 11, 75231 Paris Cedex 05, France*
[7] *Sensor Laboratory, Department of Information Engineering (DII), University of Brescia, Via Valotti 9, 25133 Brescia, Italy*
[8] *National Center for Biomedical Engineering, Technical University of Moldova, 168 Stefan cel Mare Av., MD-2004 Chisinau, Republic of Moldova*
[9] *Department of Nanoelectronics and Surface Modification, Sumy State University, 2, Rymskogo-Korsakova Str., 40007 Sumy, Ukraine*
[10] *Department of Earth Sciences, Utrecht University, Budapestlaan 4, 3584 CD Utrecht, The Netherlands*

[†] Corresponding authors:
Prof. Dr. O. Lupan, (ollu@tf.uni-kiel.de ; oleg.lupan@mib.utm.md)
Kiel University, Germany; Technical University of Moldova, Moldova; UCF, U.S.A.

Prof. Dr. R. Adelung, (ra@tf.uni-kiel.de)
Kiel University, Germany

Dr. S. Hansen, (sn@tf.uni-kiel.de)
Kiel University, Germany

Prof. Dr. F. Faupel, (ff@tf.uni-kiel.de)
Kiel University, Germany

Dr. David Santos-Carballal (d.santos-carballal@leeds.ac.uk)
University of Leeds, United Kingdom.

Cite this paper as : O. Lupan, D. Santos-Carballal, N. Ababii, N. Magariu, S. Hansen, A. Vahl, L. Zimoch, M. Hoppe, T. Pauporté, V. Galstyan, V. Sontea, L. Chow, N. H de Leeuw, F. Faupel, R. Adelung, E. Comini, $TiO_2/Cu_2O/CuO$ Multi-nanolayers as Sensors for H_2 and VOCs: An Experimental and Theoretical Investigation.
ACS Appl. Mater. Interfaces 13 (2021) 32363–32380.

ABSTRACT

Highly sensitive $TiO_2/Cu_2O/CuO$ multi-nanolayers have been grown in various thicknesses by a cost-effective and reproducible combined spray-sputtering-annealing approach. The ultra-thin TiO_2 films were deposited by spray pyrolysis on top of sputtered-annealed Cu_2O/CuO nanolayers to enhance their gas sensing performance and to improve their protection against corrosion at high operating temperatures. The prepared heterostructures have been investigated using scanning electron microscopy (SEM), X-ray diffraction (XRD), ultraviolet visible (UV-Vis) and microRaman spectroscopy. The gas sensing properties were measured at several operating temperatures, where the nanolayered sensors with oxide thicknesses of between 20 and 30 nm (Cu_2O/CuO nanolayers) exhibited a high response and excellent selectivity to ethanol vapour only after thermal annealing at 420°C. The results obtained at an operating temperature of 350 °C demonstrate that the CuO/Cu_2O nanolayers with a thickness between 20 and 30 nm are sensitive mainly to ethanol vapour, with a response of ~150. The response changes from ethanol vapors to hydrogen gas as CuO/Cu_2O nanolayers thickness changes from 50 nm to 20 nm.

Density functional theory-based calculations were carried out of the geometries of the $CuO(\bar{1}11)/Cu_2O(111)$ and $TiO_2(111)/CuO(\bar{1}11)/Cu_2O(111)$ heterostructures and their sensing mechanism towards alcohols of different chain lengths and molecular hydrogen. The reconstructed hexagonal $Cu_2O(111)$ surface and the reconstructed monoclinic $CuO(\bar{1}11)$ and $TiO_2(111)$ facets, all terminated in an O layer, lead to the lowest surface energies for each isolated material. We studied the formation of the binary and ternary heteroepitaxial interfaces for the surface planes with the best matching lattices. Despite the impact of the $Cu_2O(111)$ substrate in lowering the atomic charges of the $CuO(\bar{1}11)$ adlayer in the binary sensor, we found that it is the different surface structures of the $CuO(\bar{1}11)/Cu_2O(111)$ and $TiO_2(111)/CuO(\bar{1}11)/Cu_2O(111)$ devices that are fundamental in driving the change in the sensitivity response observed experimentally.

Cite this paper as : O. Lupan, D. Santos-Carballal, N. Ababii, N. Magariu, S. Hansen, A. Vahl, L. Zimoch, M. Hoppe, T. Pauporté, V. Galstyan, V. Sontea, L. Chow, N. H de Leeuw, F. Faupel, R. Adelung, E. Comini, $TiO_2/Cu_2O/CuO$ Multi-nanolayers as Sensors for H_2 and VOCs: An Experimental and Theoretical Investigation.
ACS Appl. Mater. Interfaces 13 (2021) 32363–32380.
The experimental data presented here, supported by the computational results, promote the use of the multi-nanolayered films tested in this work as reliable, accurate and selective sensor structures for the tracking of gases at low concentrations.

KEYWORDS: Nanolayers, Nanomaterials, Multilayered Films, CuO, *p*-type, Cu_2O, TiO_2, sensor

1. Introduction

Functional nanomaterials, including semiconducting oxide heterostructures with tunable performances, are an essential part of semiconductor-powered devices. However, synthesizing such nanocomposites has to be highly specific with respect to phase control at the nanoscopic level. Heterojunctions between different semiconductor oxide nanocrystals, especially based on ultrathin films with mixed phases, may improve the characteristics of gas sensors due to their unique detecting mechanism [1–4]. The specific features of the heterojunction in nanocrystalline multi-layered composites is crucial to control the gas sensing characteristics, i.e. selectivity and gas response of the sensor, as a result of the top surface and interface phenomena [1,5,6]. A seminal work by Brattain and Bardeen [7] reported that gas adsorption on semiconducting surfaces produces a change of its electrical conductance [7], which has contributed to the further development of the sensor industry based on solid state materials.

From the nanotechnology point of view, metallic copper (Cu) and its oxides have received much attention due to their variety of real applications, particularly in the field of new nanotechnology components for microelectronics [4,8,9]. Copper oxides are *p*-type semiconducting oxides and can be obtained in forms such as cuprite (Cu_2O) and cupric oxide (CuO), which depends

on the valence state of copper. The cuprous oxide cuprite (Cu_2O) is amongst the earliest semiconducting oxides used in solid state electronics [6,10,11]. Although cuprite has been the focus of numerous experimental and theoretical studies [1,7,12–14], including its vibrational and optical properties, the electronic properties of Cu_2O continue to puzzle the scientific community. As applications of Cu_2O in nanoelectronics, photovoltaics, solid-state electronics, biosensing and spintronics emerge,[4,9,15] as well as light-driven purification of wastewater,[8] understanding at the atomic level of the electronic structure of Cu_2O is important for the control its properties and of identification of future applications in devices or nanodevices.

CuO has a band gap in the range 1.2 – 2.1 eV, with *p*-type semiconducting properties[12] with significant potential for sensing applications, especially in mixed CuO/Cu_2O phases [6,11]. A summary of gas sensor structures based on copper oxide nanomaterials can be found in several reviews [16–20].

The (111) surface has been found, both in simulations [13,21] and experimentally [22], to be the most stable cuprite (Cu_2O) plane under a range of different conditions. Furthermore, the almost complementary $(\bar{1}11)$ facet was observed to be highly prominent in the crystals of the more oxidised tenorite (CuO) phase [23]. Although less stable than other planes, the anatase TiO_2(111) surface has been reported as one of the most reactive for photocatalytic applications [24] and in H_2 evolution [25].

Inorganic UV absorbers such as TiO_2, ZnO and CeO_2 are generally employed in shielding applications for the ultraviolet (UV) protection of different surfaces [26,27], where effective physical nano-coating barriers are needed for high temperature applications [28]. Titania (TiO_2) nano-coatings are used extensively to increase surface hardness and adhesive strength; to provide long term and high temperature protection against corrosion; to enhance tribological properties; and to improve the design of the transparent coatings of self-cleaning surfaces [27–30].

Cite this paper as : O. Lupan, D. Santos-Carballal, N. Ababii, N. Magariu, S. Hansen, A. Vahl, L. Zimoch, M. Hoppe, T. Pauporté, V. Galstyan, V. Sontea, L. Chow, N. H de Leeuw, F. Faupel, R. Adelung, E. Comini, $TiO_2/Cu_2O/CuO$ Multi-nanolayers as Sensors for H_2 and VOCs: An Experimental and Theoretical Investigation.
ACS Appl. Mater. Interfaces 13 (2021) 32363–32380.

Detection and discrimination of volatile organic compounds (VOCs), which are classified as hazard vapors with adverse short- and long-term consequences on the environment and human health [31], is important in the continuous monitoring of indoor air quality, which therefore requires reliable sensors. Moreover, exhaled VOCs can serve as biomarkers to assist in the non-invasive identification of various diseases. For example, acetone indicates diabetes [14,32–35], whereas isoprene, toluene, and acetic acid are signals of lung cancer, [31,36–38] and breath testing is therefore a highly promising approach for non-invasive cancer screening [39]. VOC analysis in patient breath offers insight into the metabolic processes in the anatomy/physiology that are altered by underlying diseases [40,41], although a detailed impression of the metabolic route leading to these molecules is still under investigation [39].

This study reports the fabrication of stable ethanol sensors using multi-nanolayered films consisting of titania/cuprite/cupric oxide ($TiO_2/CuO/Cu_2O$/glass). The cuprite/cupric oxide structures are produced by a method based on sputtering combined with thermal annealing, before spraying titania on the surface of the CuO/Cu_2O/glass substrate. Interdigitated Au-electrodes are deposited on the top surface of the specimens to connect heterostructures and perform gas sensing tests, and the morphology composition, structure, electrical transport and gas sensing properties of the materials are studied. Moreover, a theoretical discussion developed from density functional theory (DFT) calculations of the binary heterojunction $CuO(\bar{1}11)/Cu_2O(111)$ and the ternary heterostructure $TiO_2(111)/CuO\ (\bar{1}11)\ /Cu_2O(111)$ have been performed. First, we have investigated the structures and relative stabilities of the hexagonal and monoclinic surfaces for each isolated material, before elucidating the arrangement of the heteroepitaxial junctions and reporting their work function values and scanning tunnelling microscopy (STM) images. The calculated values of the work function rationalise the reactivity trends of the binary and ternary heterojunctions, whereas their computed STM images compare well with the experimental SEM

images. The adsorption energies have been computed for molecular hydrogen (H_2), ethanol (C_2H_5OH) and *n*-butanol (*n*-C_4H_9OH) and we have plotted the electron charge density flow after the interaction with the heterojunctions in order to interrogate their selectivity changes.

2. Experimental Section

Glass slides from ThermoScientific (2.5 × 7.5 cm) were employed as the substrates for the device development. The glass substrates were cleaned by dipping in HCl (11%) and then rinsed with distilled H_2O and acetone for 11 min, which was followed by ultrasonic bath in ethanol for 11 min and then rinsed in deionized H_2O [1,42]. Afterward, the CuO-Cu_2O ultrathin layers with thicknesses of 20, 30, 40, 50 and 60 nm were prepared on top of the clean glass by sputtering metallic copper under vacuum conditions. The Cu sputtering was carried out using a custom-built RF-magnetron system at 25°C, a pressure of 3.6×10^{-3} mbar, an Argon gas flux of 22 sccm and a power of 51 W. Evochem GmbH, Germany supplied the copper metal (with high purity: 5n = 99,999%, radius of 2.5 cm). The deposition rate of 6 nm/min was determined experimentally by using a profilometer. Then, the metallic copper layers deposited on the glass substrates were thermally treated at 420°C under normal atmospheric conditions for 30 or 60 min. The temperature for the thermal treatment was in accordance with our previous work of the ultrathin mixed CuO-Cu_2O oxide film [6,43]. Five different sample sets were produced with thicknesses of 20, 30, 40, 50 and 60 nm for the CuO-Cu_2O layer on the microscopic glass substrate. Next, titania (TiO_2) films were spray-pyrolysis-deposited on top of the mixed copper oxide phase layers to prepare another five sample sets. Afterwards, all materials were mounted on a thermal heating plate, where we kept the temperature at 420°C for 25 min prior to starting the spray pyrolysis process, as published previously by Pauporté *et al*. [27,42,44]. For the spray pyrolysis, the precursor was delivered as a mixture of 7.1 ml

of isopropanol, 0.62 ml of titanium (IV) tetra-isopropoxide (TTIP) and 0.41 ml of acetylacetone. The carrier gas used was an oxygen flow, which was selected as previously reported [42,44], in order to blow the mixed aerosol through a valve with a diameter of 10 mm directly on the surface of CuO/Cu_2O/glass composite, which remained on the heated hot plate at 420°C for the entire spray process. The CuO/Cu_2O samples were grown with different thicknesses of 20, 30, 40, 50 and 60 nm, labeled as Cu20, Cu30, Cu40, Cu50 and Cu60, respectively. Afterwards, the $TiO_2/CuO/Cu_2O$ heterostructures were treated under air at 420°C for another 30 min (Cu20, Cu30, Cu40) or 60 min (Cu50, Cu60), depending on their thickness, prior to allowing them to cool down spontaneously. The thickness of the TiO_2 layer was monitored throughout the duration of the spray, as reported before [42,44].

After the preparation of materials, Au electrodes were grown on top of the nanolayered $TiO_2/CuO/Cu_2O$ samples through an Al meander-shaped mask [6,43]. The Au top-contacts have a thickness of is ~ 180 nm and a separation of 1 mm between gold contacts. The Au target (purity: 4n = 99,99%, radius: 2.5 cm) which was produced by Evochem GmbH, Germany, was mounted on the magnetron (DC). The chamber pressure during Au sputtering was 3.55×10^{-3} mbar, whereas the flowrate of Ar was about 16 sccm and the power of sputtering was set at 51 W, enabling a deposition rate of about 47 nm/min [42]. The morphological, structural, chemical, micro-Raman (MR) measurements and X-ray photoelectron spectroscopy (XPS) investigations were carried out as before [1,45]. MR experiments were done using a Raman WITec Alpha300 RA spectrometer at 22°C, as reported before [46]. A graphite monochromatized CuK_1 radiation (1.5405 Å) at 40 kV and 40 mA were used for the X–ray diffraction (XRD), which was carried out using a Seifert 3000 TT instrumenr, [33] and X-ray photoelectron spectroscopy (XPS) was used to measure the thickness of the TiO_2/CuO thin films by using an Omicron Nano-Technology GmbH, Al-anode, P=240 W, as reported previously [42]. We charge calibrated the documented spectra using the signal at 284.5

eV corresponding to the aliphatic carbon C-1s and the "CasaXPS", software version 2.3.16. We employed a Varian Cary 5000 spectrophotometer to carry out the characterization of the optical properties of the samples, where we used the integrating sphere supplied in the wavelength values between 300 and 2500 nm, as before [47]. The gas detection characteristics were obtained using the set-up and protocol described previously [6,43,48,49] at 30% relative humidity (RH). A computer-controlled Keithley2400 sourcemeter at 0.25 V applied bias voltage was used to record continuously the electrical measurements, which were processed through the LabView software (from National Instruments). The responses to gas and VOCs were defined as the ratio ($\frac{R_g - R_a}{R_a} \cdot 100\%$), where R_g and R_a - the electrical resistances of the specimens exposed to gas/VOC and air under normal environmental conditions, respectively [6,43].

The surface properties of the binary and ternary heteroepitaxial interfaces were simulated using unrestricted density functional theory (DFT) simulations, which are described in **Text S1** (Supporting Information).

Figure 1 shows the technological flow for the manufacture of the mixed-phase: (a) CuO/Cu_2O (Final device set #1), and (b) $TiO_2/CuO/Cu_2O$ (Final device set #2) nanofilm devices. The general process can be described as follows: Step 1; Pre-cleaned glass substrate is sputtered with copper nanoparticles with a radius of about 2-5 nm to obtain ultrathin films of copper with thicknesses between 20 and 60 nm; Step 2; thermal annealing in a furnace at the temperature of 420°C for 30 min (for sample sets Cu20, Cu30 and Cu40) or 60 min (for sample sets Cu50 and Cu60) in air to develop the CuO/Cu_2O nanolayer-heterojunctions. Steps 3 and 4 in **Figure 1a** are the deposition of the Au contacts by shading a metallic meander mask with a 1 mm gap. In step 5, we obtain the device 1 based on the CuO/Cu_2O nanolayers. Following steps 3 and 4 in **Figure 1b**, where the thin films of TiO_2 are deposited with a thickness of 20 nm and then thermally treated in a furnace at the temperature of 420°C for 30 min (for sample sets Cu20, Cu30 and Cu40) or 60

min (for sample sets Cu50 and Cu60) in air, we obtain the sensitive multi-nanolayered $TiO_2/CuO/Cu_2O$ heterojunction film. Steps 5 and 6 in **Figure 1b** are the deposition of the Au contacts as in **Figure 1a**. Finally, step 7 represents the final device set #2, i.e. the $TiO_2/CuO/Cu_2O$ heterostructure. It is important to mention that the layers are drawn as straight lines in **Figure S1** but, in reality, they are rough polycrystalline layers (**Figure 2**). **Figure S1** displays the cross-section view of the devices from the set #1 made of CuO/Cu_2O nanolayers (Device 1), and set #2, which are based on heterolayers of $TiO_2/CuO/Cu_2O$ heterolayer films (Device 2).

3. Results and Discussion

3.1. Morphology and composition analyses

Figure 2a-f presents the low and high (in the insets) magnification SEM images of the nano-crystallite CuO/Cu_2O samples, which were grown using the reproducible spraying/sputtering/annealing approach, owing to the possibility of controlling the speed of sputtering growth. We thus obtained five samples simultaneously from a single substrate before thermal annealing at 420°C for 30 min (for sample sets Cu20, Cu30 and Cu40) or 60 min (for sample sets Cu50 and Cu60) in air. It can be clearly observed that the volume of nanoparticles esentially changes with the film thickness, which also affects the sensing properties. For the CuO nanoparticles, their larger electrical conductivity leads to some bright dots, which are seen in **Figure 2a-c,**[43] in the areas exposed to the electron beam of the SEM. The nanoparticles, which appear much smaller in size in the SEM images due to thinner films, oxidize completely during the 30 min of annealing.

The ultra-thin films possess very good adhesion to the microscopic glass substrates, as we have not seen any signs of delamination during the three years that we have been investigating these types of samples [1,12].

3.2. X-ray photoelectron spectroscopy and Micro-Raman characterization

For the $TiO_2/CuO/Cu_2O$ layered thin films sensor, the X-ray photoelectron spectra (XPS) is presented in **Figure 3**, where the overview spectrum, shown in **Figure 3a**, attests to the presence of the Cu, O, Ti, Na and C elements. Cu, O and Ti originate from the TiO_2/CuO layers whereas the signal from carbon is as reported before [1,48]. The Na peak corresponds to the glass substrates [42] used for the deposition of the sensor structures, since samples were cut for XPS.

High-resolution Cu-2p and Ti-2p lines are depicted in **Figure 3b**. A closer look at the Cu-2p line clearly reveals the Cu-$2p_{1/2}$ and Cu-$2p_{3/2}$ satellite lines, which are shifted to higher binding energies. The observed satellite peaks in the spectrum are commonly noted a signature for the presence of CuO, [43,50] which is found in the base layer of our samples.

The signals between 459.6 - 458.0 eV are due to Ti-$2p_{3/2}$, which is usually assigned to Ti in TiO_2. The evaluation of the high resolution Ti-2p XPS spectra reveals that the line at 458.3eV corresponds to Ti-$2p_{3/2}$. The separation of 5.6 eV between the Ti-$2p_{3/2}$ and Ti-$2p_{1/2}$ peaks and the position of the Ti-$2p_{3/2}$ signal, illustrate the presence of Ti as TiO_2 in the base layer, according to the literature [51,52].

The Raman scattering method is a useful spectroscopic technique to measure the vibrational modes and phase of ultra-thin layers and nanomaterials, owing to its ability to determine the vibrational modes of the heterostructure [11,45]. Micro-Raman spectroscopy was employed to investigate the characteristics at the nano-scale, namely the lattice dynamics

(electron-phonon interaction) of the CuO/Cu_2O and $TiO_2/CuO/Cu_2O$ nano-materials. The micro-Raman spectra in the range 100-1000 cm^{-1} were obtained at room temperature for the CuO/Cu_2O and $TiO_2/CuO/Cu_2O$ nano-materials, as shown in **Figure S2** and **Figure S3**.

The Raman studies clearly show the formation of the mixed copper oxide phases, namely CuO/Cu_2O, following thermal annealing at 420°C under ambient conditions, as well as the $TiO_2/CuO/Cu_2O$ heterostructure after spraying a TiO_2 nano-layer on top of the binary films, which show the existence of heterostructured mixed phase films. A detailed description of the aforementioned results is given in **Text S2** (Supporting Information).

3.3. Ultraviolet, Visible and Near Infrared spectroscopy

Ultraviolet, Visible and Near InfraRed (UV-Vis-NIR) absorption spectroscopy is a characterization method used to study energy level as well as optical properties of transparent semiconducting oxide materials. The room temperature spectra of the CuO/Cu_2O and $TiO_2/CuO/Cu_2O$ heterostructures allowed the detection of the optical absorption and excitonic transitions characteristic of the nanolayers. The transmission and absorption spectra are presented in **Figure S4**, and the plots of the $(\alpha hv)^2$ *versus* the photon energy (hv) for the CuO/Cu_2O and $TiO_2/CuO/Cu_2O$ heterostructures are shown in **Figure S5** and **Figure S6**. More details of the UV-Vis-NIR characterization are provided in **Text S3** (Supporting Information).

3.4. Gas sensing properties

First, we will focus on the CuO/Cu_2O samples and their gas sensing performances, followed by the gas sensing performances of the $TiO_2/CuO/Cu_2O$ nanolayered materials, which we will compare to the base layer.

Gas sensing results of CuO/Cu₂O. The CuO/Cu₂O based Cu20, Cu30, Cu40, Cu50 and Cu60 nanolayer samples were connected in the sensor structures as indicated schematically in **Figure S1**.

Figure 4a represents the responses at the standard deviations between multiple measurements of the CuO/Cu₂O samples to hydrogen and ethanol, at the operating temperature of 350°C, from which it is clear that Cu20 and Cu30 samples show the highest response to ethanol. From **Figure 4a** we observe that, for all thicknesses, the CuO/Cu₂O specimens are more selective to ethanol compared to the other tested gases (hydrogen, ethanol, 2-propanol, *n*-butanol, acetone and ammonia). However, the response and selectivity of the sensors decrease as the thickness of the layers increases (more than 30-40 nm), because with increasing thickness of the layers, the electrical resistance of the structures decreases, which is in accordance with previously reported data [6]. The optimum thickness is therefore in the range 20−30 nm (sample sets Cu20 and Cu30). The response values of CuO/Cu₂O nanolayers to different analytes are depend on their thickness, specifically when the thickness is in the order of the Debye length [43,53]. The sensing mechanism proposed for these results from the binary heterostructure is explained in **Text S4** (Supporting Information).

Figure 4b represents that the current-voltage (*I-V*) curves of the prepared structures, and from **Figure S7a**, it can be seen that the characteristics are linear at room temperature for all samples. According to the data in **Figure 4b and Figure S7a**, the *I-V* characteristics for all the CuO/Cu₂O samples of different thicknesses show Ohmic contact behavior between the CuO/Cu₂O nanolayers and the Au top contact at room temperature. However, at the operating temperature of 350 °C (**Figure S8a**) the *I-V* current-voltage characteristics is non-linear, which can be attributed to a conductivity effect driven by the energy barrier. The variation of the electrical current with temperature, see **Figure 4c**, indicates that the heterostructure is also convenient for temperature

measurement. We have used equation (1) to express the electrical resistivity of our *p*-type semiconducting oxides [54]:

$$\rho \equiv \frac{1}{\sigma} = \frac{1}{q\mu_p p} = \frac{1}{q\mu_p\left(N_V e^{\left[-\left(\frac{E_F - E_V}{KT}\right)\right]}\right)} = \frac{e^{\left(\frac{E_F - E_V}{KT}\right)}}{\sigma\mu_p N_V} \quad (1)$$

where ρ is the electrical resistivity, σ is the electrical conductivity, q is the charge of the electron, μ_p is the holes mobility, p is the holes concentration, N_V is the acceptors concentration, E_F is the Fermi energy, E_V is the maximum energy of the valence band, T is the absolute temperature and k is the Boltzmann constant.

The response variation of the structures to 100 ppm of ethanol as a behavior of the operating temperature was studied to find the optimal working conditions. **Figure 4c** shows the response of a Cu20 (CuO/Cu_2O sample) to different gaseous compounds (hydrogen, *n*-butanol, 2-propanol, ethanol, acetone and ammonia) at the operating temperatures between 250−350 °C. The standard deviation between multiple measurements of the same sample set is indicated with error bars. For ethanol vapors, the response of the sensor at 350 °C is larger compared to the other gases. Sample sets tested at 250, 300 and 350 °C have the highest response to ethanol with values of about 24%, ~121% and ~140%, respectively, whereas **Figure 4c** also shows that the hydrogen response improved with the operating temperature. The sensing response of the CuO/Cu_2O heterostructure with a thickness of between 20 and 30 nm demonstrates the *p*-type behavior of this material. The response variation of the structure to 100 ppm of ethanol depending on its operating temperature was investigated to find the optimal working conditions, **Figure 4d** indicates the dynamic response of the Cu20 sample to 100 ppm of ethanol. We observe that the response time (t_r) and recovery time (t_d) are relatively small under the operating temperatures of 250 °C, 300 °C and 350 °C (t_r = 18.8, 13 and 18.5 s, t_d = 43.3, 46.4 and 49.6 s, respectively). Then, we have prepared more complex

structures based on $TiO_2/CuO/Cu_2O$ and studied their sensing properties towards H_2 and ethanol. After this, the effect of each layer can be explained in detail.

Gas sensing performances of $TiO_2/CuO/Cu_2O$. The hydrogen and ethanol responses of the samples consisting of the $TiO_2/Cu_2O/CuO$ multi-nanolayered films with different thicknesses are studied to determine the impact of adding TiO_2 to the top layer. The ternary heterojunction can also act as a self-cleaning surface or to enhance the gas detection and to improve the protection against corrosion at high temperatures [27–30,55,56].

Figure 5a shows the response to hydrogen and ethanol of the $TiO_2/CuO/Cu_2O$ Cu20, Cu30, Cu40, Cu40 and Cu60 samples, measured at the operating temperature of 350 °C. From **Figure 5a** we can see that the $TiO_2/CuO/Cu_2O$ Cu20 and Cu30 samples are more sensitive towards ethanol compared to the hydrogen gas. However, increasing the thickness of CuO/Cu_2O to Cu50 and Cu60 changes the sensing performance of $TiO_2/CuO/Cu_2O$ structures and the most sensitive gas becomes to hydrogen, although the response values are smaller. However, the response values of sensors with the thicker layers of CuO/Cu_2O are lower towards hydrogen and ethanol compared to that of Cu20 and Cu30. The best sensing performances to ethanol were obtained for the samples with the thickness of 30 nm (sample Cu30). **Figure 5b** illustrates the electrical current-voltage plot of the $TiO_2/CuO/Cu_2O$ samples, and the linear Ohmic behavior at room temperature can be seen in **Figure S7b.** However, as already stated, at the operating temperature of 350 °C (**Figure S8b**) the *I-V* current-voltage characteristics is non-linear due to a conductivity effect driven by the energy barrier. **Figure 5c** presents the responses to different chemical compounds (hydrogen, ethanol, 2-propanol, *n*-butanol, acetone and ammonia) versus the operating temperature of the $TiO_2/CuO/Cu_2O$ Cu20 sample set. At all operating temperatures, i.e. 250 °C, 300 °C and 350 °C, we see that the samples have the highest response to ethanol with responses of ~38%, ~115% and ~121%, respectively. Comparatively (the data in **Figure 4c** and **Figure 5c**), the response value

was enhanced with increasing operating temperatures for the $TiO_2/CuO/Cu_2O$ nanomaterial. Thus, there was no noticeable response for these sensor-structures below OPTs of 250 °C due to surface reactions with different oxygen species. The maximum response is achieved at an operating temperature of 350 °C, which is the highest temperature allowed by our gas test equipment. **Figure 5d** indicates the dynamic response to 100 ppm of ethanol of the $TiO_2/CuO/Cu_2O$ samples (prepared based on the Cu20). For the working temperatures 250, 300 and 350 °C, we observed that the response times (τ_r) are 18.9, 16.3 and 13.8 s) and recovery times (τ_d) are 35.5, 28.3 and 37.3 s, respectively) are relatively low.

Comparison of the gas sensing features of Cu_2O/CuO and $TiO_2/Cu_2O/CuO$. Here we compare the gas response of the multi-nanolayered Cu_2O/CuO and $TiO_2/Cu_2O/CuO$ heterostructured films.

Comparing the data in **Figure 4c** and **Figure 5c** indicates that the response to hydrogen has increased for the ternary system with respect to the heterojunction at all operating temperatures. **Figure 6a** represents the relationship between the response to 100 ppm of ethanol vapors and the power consumption versus the applied voltage for the CuO/Cu_2O Cu20 samples. **Figures 6a** and **6b** show that when the applied bias voltage decreases, the response to the ethanol vapors increases and the power consumption decreases, which effect can be attributed to the nonlinear I-V current-voltage characteristics at OPT 350 °C (**Figure S8a** and **S8b**). For an applied bias voltage of 0.5, 0.01 and 0.005 V, the power consumption is about 88, ~0.02 and ~0.004 μW (approximately 4 nW), and response is about 140%, ~160% and ~300%, respectively. This power consumption is part of the energy consumption of the entire sensor system, because the energy consumption to heat the sample to OPT 350 °C is not calculated here.

Figure 6b represents the response to 100 ppm of ethanol vapors and the dependence of the power consumption versus the applied bias voltage for the $TiO_2/CuO/Cu_2O$ Cu20 sample set. This

figure shows that when the applied voltage decreases, the power consumption also decreases. For example, the power consumption is about 1.5, ~0.33, ~0.05 and ~0.001 μW (approximately 1 nW) at the applied voltage of 0.25, 0.1, 0.05 and 0.01 V, respectively. However, the gas response is ~120% for the applied bias voltage of 0.25 V, which decreases to ~97% under 0.1 V of an applied bias voltage, which increased to ~ 160% and ~222% at the applied bias voltage to 0.05 V and 0.01 V, respectively.

Figure 6c represents the variation of the response of the CuO/Cu_2O Cu20 (curve 1) and $TiO_2/CuO/Cu_2O$ Cu20 (curve 2) samples to 100 ppm of ethanol vapors for 105 days. **Figure 6c** shows that the response to ethanol vapors has bisected for the (curve 1) samples, whereas it remained unchanged in the case of the $TiO_2/CuO/Cu_2O$ (curve 2) samples significant changes were not observed due to the self-cleaning effect of the ternary heterostructure [55,56].

According to the results presented in this study, changes in the conductance of semiconductor oxide-based chemical sensors are caused by interactions with environmental chemical compounds with the sensor surface, which are strongly influenced by the operating temperature [2,57]. An efficient way to improve the characteristics of the sensor is through control of the catalytic properties of the oxide surface [2,42].

Figure 7 shows the gas response to 1, 5, 10, 50, 100, 500 and 1000 ppm ethanol () versus the type of CuO/Cu_2O and $TiO_2/CuO/Cu_2O$ samples Cu20, Cu30, Cu40, Cu50 and Cu60 measured at the working temperature of 350 ^oC. **Figure 7** suggests that all samples responded to all concentrations of ethanol.

Figure 8 shows the dynamic response of the CuO/Cu_2O (**Figure 8a**) and $TiO_2/CuO/Cu_2O$ (**Figure 8b**) samples with the thickness of 20 nm (Cu20) and 30 nm (Cu30) to 1, 5, and 10 ppm of ethanol at 350 ^oC of working temperatures. From the plot it can be seen that the response of the sensors is quite high at very low concentrations of ethanol. The sensing parameters of CuO/Cu_2O

and $TiO_2/CuO/Cu_2O$ samples with the thickness of 20 nm (Cu20) and 30 nm (Cu30) at operating temperature of 350 ^oC to 1, 5, and 10 ppm of ethanol are shown in **Table S1**. For the CuO/Cu_2O and $TiO_2/CuO/Cu_2O$ Cu20 and Cu30 samples, the dynamic response to 1 ppm of ethanol is shown in **Figure S9**.

The dynamic response to various concentrations of ethanol (1, 5, 10, 50, 100, 500 and 1000 ppm) by the CuO/Cu_2O and $TiO_2/CuO/Cu_2O$ Cu20 and Cu30 samples is shown in **Figure S10**. The gas response to high concentrations of hydrogen is presented in **Figure S11**, which shows the effect of different concentrations of hydrogen (100, 500 and 1000 ppm) versus the type of CuO/Cu_2O and $TiO_2/CuO/Cu_2O$ Cu20, Cu30, Cu40, Cu50 and Cu60 sample sets measured at 350 ^oC of working temperature. **Figure S11** displays that the response of the samples increases strongly at high concentrations of hydrogen.

Overall, the chemical detection mechanism proposed for CuO/Cu_2O relies on surface physico-chemical reactions, which strongly depend on the operating temperature. More details of the gas detection mechanism are described in **Text S4** (Supporting Information) and the energy band diagrams of heterostructures $TiO_2/CuO/Cu_2O$ in air and ethanol vapors are represented in **Figure S12**.

3.5. Simulation of bulk phases

We first investigate the optimised bulk structures of the materials used to build the heteroepitaxial structures, which are later used to simulate the molecular adsorption to compare with our experiments. Our starting point for the substrate is Cu_2O, characterised by the space group $Pn\bar{3}m$ (no. 224) and the cuprite structure, with Cu in the lowest oxidation state of 1+ [58]. Erreur ! Source du renvoi introuvable.**Figure 9a** presents the conventional cubic unit cell of Cu_2O with two formula units (f.u.). The O atoms are distributed in a body-centred cubic (*bcc*) sublattice, whereas

the Cu ions are arranged in a face-centred cubic (*fcc*) sublattice. The 2-fold Cu atoms occupy the 4*b* Wyckoff linear positions with coordinates at the origin of the unit cell, while the 4-fold O ions occupy the 2*a* tetrahedral crystallographic sites at (¼, ¼, ¼). CuO, the material in the middle of the ternary heterostructure with Cu in the higher oxidation state of 2+, crystallises in the tenorite structure with space group $C2/c$ (no. 15) [59]. **Figure 9b** shows the conventional monoclinic unit cell of CuO with 4 f.u. In this structure, the 4-fold Cu atoms are located at the 4*c* Wyckoff square planar positions with coordinates (¼, ¼, 0), whereas the 4-fold O O counter-ions fill the 4*e* distorted tetrahedral holes at (0, *y*, ¼). CuO forms two sets of $^{1}_{\infty}[CuO_{4/2}]$ chains perfectly aligned along the [110] and $[1\bar{1}0]$ directions [60]. The deviation of the *y* value from ½, in fractional coordinates, represents the staggering of the $^{1}_{\infty}[CuO_{4/2}]$ chains along the [001] direction. The crystal structure of anatase TiO_2, the topmost material in the ternary heterojunctions, is tetragonal with space group $I4_1/amd$ (no. 141) [61]. The conventional unit cell contains 4 f.u. of TiO_2, as depicted in **Figure 9c**. The distorted octahedral Ti^{2+} cations are in the 4*b* crystallographic positions with coordinates (0, ¼, 3/8), and the O anions are in the 8*a* distorted trigonal planar sites at (0, ¼, 1/6). The anatase TiO_2 structure displays channels in the [100] and [010] directions and dual chains $^{1}_{\infty}[TiO_{6/2}]$ along the [2,2,13] direction.

Table S2 shows the optimised and experimental lattice parameters for the cubic unit cell of Cu_2O, the monoclinic unit cell of CuO and the tetragonal unit cell of TiO_2. Our calculations indicate that the lattice parameters were overestimated by 0.41% for CuO [59] and by 1.59% for TiO_2 [61], while it was underestimated by 0.28% for Cu_2O [58]. The internal coordinates of the three materials were allowed to relax, with all ions showing a large preference for staying in their perfect Wyckoff crystallographic positions. The value calculated for the parameter *y* is 0.004 larger than in experiments, indicating that we predict a smaller staggering for the $^{1}_{\infty}[CuO_{4/2}]$ chains along the

[001] direction in the simulated cell of CuO. The shapes of the conventional unit cells were fully optimised, but Cu_2O, CuO and TiO_2 remained in the ideal cubic, monoclinic and tetragonal structures, respectively. The perfect match between the simulated and experimental angle β further supports the undistorted monoclinic shape of CuO. More details and a description of the atomic Bader charges, atomic magnetic moments and band gaps are provided in **Text S5** (Supporting Information).

3.6. Simulation of isolated surfaces

We have also simulated the pristine $Cu_2O(111)$ surfaces with hexagonal symmetry as well as the $CuO(\bar{1}11)$ and $TiO_2(111)$ facets with monoclinic symmetry, that were used to construct the binary and ternary heterojunctions. The surface slabs were constructed using METADISE [62] to cut the geometry optimized bulks. A vacuum gap of 20 Å was added above the surfaces to avoid spurious interactions between the periodic supercells. The two bottommost layers were kept at their relaxed atomic bulk positions, to simulate the bulk phase, while the rest of the slab was allowed relax explicitly. We have applied dipole corrections in the direction perpendicular to the surface [63,64] to improve the description of the total energy of our single surface models [65–69]. According to this formalism, a planar dipole sheet was introduced in the centre of the vacuum region, and its strength was calculated self-consistently to compensate the artificial adsorbate-induced dipole.

The $Cu_2O(111)$ and $CuO(\bar{1}11)$ surface slabs have the smallest surface areas of 31.378 and 32.438 $Å^2$, respectively. The surface cell of Cu_2O contains 24 atoms, whereas CuO comprises 32 atoms distributed in four stacking sequences consisting of 2 and 4 f.u., respectively. The $TiO_2(111)$ surface was modelled using a slab with an area of 54.580 $Å^2$ and 36 atoms occupying 12 stacking sequences of a single stoichiometric unit each. With this setup, we ensured that all surfaces were symmetric along the *z* axis and their widths were between 7.4 and 10.1 Å. The vacuum thickness

as well as the total and relaxed number of surface layers were carefully tested until convergence to within 1 meV per atom was reached.

The stacking of the atomic layers is (O)−(Cu_4)−(O) for the Cu_2O surfaces in the (111) direction, with the atoms within parenthesis lying approximately in the same plane as shown in **Figure S13**. Termination *A* is a type 2 Tasker surface [70], with a top surface layer that has a bulk-like structure terminated in 3-fold under-coordinated O atoms and an 0.25 monolayer (ML) of monocoordinated Cu atoms with a single dangling bond. Termination *B* is a reconstructed type 3 Tasker surface [70], where the dipole moment was quenched by shifting half of the mono-coordinated Cu atoms from the topmost stoichiometric stacking sequence at the relaxed to the unrelaxed side of the slab, which created 2-fold O anions. Following relaxation of termination *A*, both the exposed 3-fold and subsurface 4-fold O atoms moved outwards by an average of 0.052 Å, while the cations migrated towards the bulk by only 42% of the displacement of the anions. We found that for termination *B*, the displacement of the atomic layers is larger than for termination *A*. The 0.5 ML mono-coordinated Cu atoms shifted their position horizontally by 0.689 Å, with half of them even coordinating the 2-fold O atoms, that only moved 0.141 Å towards the vacuum. This surface reconstruction and atomic displacements effectively increased the coordination number of both the exposed O and Cu atoms for the relaxed termination *B*.

Despite their different crystal structures, the stacking of the atomic layers for CuO in the $(\bar{1}11)$ direction is similar to Cu_2O in the (111) direction, except for their different stoichiometric ratios, as illustrated in **Figure S14**. Unsurprisingly, both terminations *A* and *B* of the CuO$(\bar{1}11)$ surface display many of the same characteristics as its $Cu_2O(111)$ counterpart. For example, termination *A* is a type 2 Tasker [70] surface presenting bulk-like structured 3-fold O and Cu atoms, of which 0.5 ML are 3-fold. Similar to the reduced copper oxide phase, the exposed atoms exhibit the lowest coordination numbers in termination *B* of CuO$(\bar{1}11)$, which is also a reconstructed type

3 Tasker surface [70]. Due to the surface construction, the 0.5 ML of Cu atoms left exposed are 2-fold, whereas 0.25 ML of the counteranions are 2-fold, 0.50 ML are 3-fold and the remaining have kept the distorted tetrahedral configuration of the bulk. After relaxation, the exposed O atoms of both terminations moved outwards by an average distance of ~0.2 Å, whereas the cations shifted horizontally their locations by 0.164 Å towards the vacuum in termination *A* and by 0.518 Å inwards in termination *B*, where they also became 3-fold.

TiO_2(111) is a type 2 Tasker surface [70] composed of thin (O)-(Ti)-(O) planes with a width of 0.220 Å and separated by 0.434 Å from the neighbouring stoichiometric units, which explains why only one termination is possible for this facet, as displayed in **Figure S15**. Cutting the bulk of TiO_2 reduces the coordination number of the exposed atoms, *i.e.* 0.5 ML of Ti become 4-fold, whereas the other half is surrounded just by three O ions, compared to the octahedral coordination environment in the bulk. Moreover, 0.75 ML of the anions are 2-fold and 0.25 ML are mono-coordinated in the freshly created surface. During relaxation, the least coordinated Ti ions moved 0.235 Å inwards. The 4-fold Ti remained approximately at the same position and the Ti of the third stoichiometric unit migrated 0.511 Å towards the surface, becoming all penta-coordinated and appearing roughly at the same layer. Moreover, all the O atoms have a coordination number of 2 after surface relaxation, with the largest average inwards displacement of 0.442 Å observed for the topmost stoichiometric unit. The anions of the third stoichiometric unit also experienced notable outwards shifts of 0.708 Å.

We have calculated the surface energy before (γ_u) and after (γ_r) relaxation as,

$$\gamma_u = \frac{E_u - n_{bulk} \cdot E_{bulk}}{2A}, \quad (2)$$

$$\gamma_r = \frac{E_r - n \cdot E_{bulk}}{A} - \gamma_u, \quad (3)$$

where n_{bulk} is the number of f.u. contained in the surface cell, E_u is the energy of the slab with all atoms at their optimised bulk positions, E_{bulk} is the energy of the bulk per f.u., E_r is the energy of

the half-relaxed slab and *A* is the surface area of one side of the slab. The degree of relaxation (*R*) was quantified as $R = 100 \cdot (\gamma_u - \gamma_r)/\gamma_u$.

From our simulation of the surface energies, which are listed in **Table S3**, we have determined that terminations *A* are the most stable for $Cu_2O(111)$ and $CuO(\bar{1}11)$, both before and after relaxation. The calculations also reveal that the overall most stable surface is $Cu_2O(111)$ with a relaxed surface energy of $\gamma_r = 70$ meV·Å^2. $TiO_2(111)$ is the least thermodynamically stable plane in this study, since its surface energy is one order of magnitude larger than for any other material. Despite their similar relaxed surface energies, termination *A* of $Cu_2O(111)$ only experiences a small degree of relaxation *R* = 4.08%, while termination *A* of $CuO(\bar{1}11)$ suffers a relaxation approximately five times larger. Termination *B* of both copper oxide surfaces have the largest degree of relaxation, in agreement with the displacement of their respective atomic layers; while the $TiO_2(111)$ facet shows a modest 9.69%. The lower charges of the undercoordinated atoms suggest that all surfaces are less ionic than their respective bulks. Our calculations indicate that the increasing order of ionic character for the surfaces is $Cu_2O(111) < CuO(\bar{1}11) < TiO_2(111)$, in line with the trend found for the charges in their respective bulk phases. The surface atoms of both $Cu_2O(111)$ and $TiO_2(111)$ are non-magnetic, as evidenced by their lack of magnetic moments. The exposed Cu atom in CuO experiences a reduction of its magnetic moment by ~0.06 μ_B atom^{-1} in terminations *A* and *B* of the $(\bar{1}11)$ surface. However, the magnetic moment is lower at 0.298 μ_B atom^{-1} and larger at 0.382 μ_B atom^{-1} for the O ions in terminations *A* and *B*, respectively, than in the bulk.

The work function (Φ), which measures the energy required to move an electron from the Fermi level (E_F) to the vacuum, was calculated as the difference between the potential of the vacuum (E_{vac}) and E_F. Based on this descriptor, the most reactive system is termination *A* of the $Cu_2O(111)$ surface, since it only requires 4.831 eV of energy to provide the electron that can

facilitate the detection of an adsorbed chemical species. However, termination *A*, which is the most stable plane of the $CuO(\bar{1}11)$ surface, has the largest work function at Φ = 5.943 eV of any of the pristine facets reported in this study. Our results suggest that the different magnetic properties and stoichiometry of the $Cu_2O(111)$ and $CuO(\bar{1}11)$ surfaces play major roles in the different trends observed for the work function values of terminations *A* and *B* of these materials. Moreover, the difference of the work function values is 0.192 eV for the least stable terminations *B* of the $Cu_2O(111)$ and $CuO(\bar{1}11)$ surfaces. Our simulated work function values suggest that $TiO_2(111)$ has an intermediate reactivity between the terminations *A* of $Cu_2O(111)$ and $CuO(\bar{1}11)$.

3.7. Simulation of the multi-nanolayers-based heterojunctions

Based on the results for the pristine surfaces, we have analysed the thermodynamic stability, atomic structure and electronic properties of the binary $CuO(\bar{1}11)/Cu_2O(111)$ and ternary $TiO_2(111)/CuO(\bar{1}11)/Cu_2O(111)$ multi-nanolayered interfaces, with hexagonal symmetry. For the binary $CuO(\bar{1}11)/Cu_2O(111)$ heterojunction, we used the 1×1 surface geometry and for the ternary heterostructure $TiO_2(111)/CuO(\bar{1}11)/Cu_2O(111)$, we employed the 1×2 supercell. Since in section 3.9 we will investigate the adsorption properties of the 2×2 ternary heterojunction interfaces, we decided to simulate these structures using 2, 1 and 4 stoichiometric stacking sequences for $Cu_2O(111)$, $CuO(\bar{1}11)$ and $TiO_2(111)$, respectively. This configuration ensures that we model 2×2 ternary heterojunctions of approximately 10.63 Å of width and containing 104 atoms, as bigger systems have a prohibitively larger computational cost. We report these heterostructures using the most stable termination *A* calculated for $CuO(\bar{1}11)$ and $Cu_2O(111)$ and the only termination of $TiO_2(111)$. All surfaces comprise incomplete top layers of O atoms, which are complementary in a “jigsaw puzzle” fashion, allowing the sub-surface Cu and Ti ions with dangling bonds to increase their coordination numbers. For the interface computations, we used

the equilibrium lattice vectors for $Cu_2O(111)$ to mimic the heteroepitaxial growth of $CuO(\bar{1}11)$ and then $TiO_2(111)$ adlayers. The $Cu_2O(111)$ is perfectly hexagonal, but $CuO(\bar{1}11)$ and $TiO_2(111)$ have monoclinic symmetries, which leads to a mismatch of their lattice parameters and angles. **Figure 10** displays the side views of the supercell slabs used to simulate the binary and ternary heteroepitaxial junctions. 50% of the exposed and 25% of the subsurface Cu atoms experience an outward relaxation of approximately 0.13 Å after the formation of $CuO(\bar{1}11)/Cu_2O(111)$, with respect to the pristine surfaces. Moreover, 50% of the subsurface anions shift their positions by ~0.22 Å towards the surface in the binary device compared to the isolated materials. Our calculations suggest that the remaining atoms in the binary heterostructure suffer only a relatively smaller displacement after the deposition of the $CuO(\bar{1}11)$ layer. Next, we have applied a layer of $TiO_2(111)$ and found that all the Ti atoms relaxed towards the bulk to roughly form a single atomic layer in the ternary heterostructure, which is similar to the atomic displacements of the pristine surface.

The scanning tunnelling microscopy images (STM) were constructed using the basic formulation of the Tersoff-Hamann approach [71] and the HIVE code [72], which has been successfully employed in previous works providing images in agreement with experiments [66,73,74]. The sign of the sample bias applied for the production of the STM image provides information of the valence of conduction bands in the vicinity of the Fermi level (E_F). For example, the positive (negative) bias of $V = 1.0$ (−0.5) eV applied for the production of the STM image of the binary (ternary) heterostructure indicates that the electrons are moving from the probe tip to the conduction band (valence band to the probe tip). The brightest spots resolved for the surface of the binary $CuO(\bar{1}11)/Cu_2O(111)$ device correspond to the protruding O atoms located at the ridges along the $[2\bar{1}\bar{1}]$ direction, as shown in **Figure 10a**. The image also resolves the O atoms situated at the grooves, whose lowest brightness can be used to evaluate their relative position with respect to

those anions at the tip of the ridge. The 3- and 4-fold Cu atoms can be seen, and their different sizes can also be used to differentiate them. **Figure 10b** clearly displays the honeycomb structure of the ternary $TiO_2(111)/CuO(\bar{1}11)/Cu_2O(111)$ interface, whose corners are defined by the O represented by the brightest spots. Although Ti are the least noticeable ions, they are still well-defined circles occupying the trigonal holes created by the O atoms.

Table S4 lists the geometric misfit parameter (ζ), which was quantified as $\zeta = 100 \cdot [1 - 2\Omega/(A_1 + A_2)]$, where Ω is the overlap area and A_1 as well as A_2 are the surface areas of the materials forming the interface [75,76]. The geometric misfit parameter is just under 1.7% for the binary heterojunction and 6.97% for the ternary interface. Note that typically, the misfit parameter is below 5% for stable heteroepitaxial junctions, but much larger values such as 18.6% and 8.3% have been measured for $ZnO(0001)/Al_2O_3(0001)$ and $MgO(111)/Al_2O_3(0001)$, respectively.[77] The values of this parameter indicate that the thin film $CuO(\bar{1}11)$ suffered a smaller compression than the expansion experienced by the TiO_2-based layer upon deposition onto the substrate.

The interfacial free energy (σ_{int}) was calculated as;

$$\sigma_{\text{int}} = \gamma_{\text{r}} + (E_{\text{int}} - n_{\text{over}}E_{\text{over}} - E_{\text{sub}})/A, \quad (4)$$

where E_{int} and E_{sub}, are the energies of the interface and substrate, respectively; E_{over} is the energy of 1 f.u. in the bulk of the overlayer; and n_{over} is the number of f.u. in the overlayer.

The interfacial free energy calculated for both heteroepitaxial systems is positive, implying that these interfaces are stable with respect to their isolated bulk components. The difference in interfacial energy for the binary and ternary heterostructures is only 21 meV $Å^{-2}$, despite the large difference of their geometric misfit parameters. Note that the interfacial free energy of the interfaces is larger and therefore less stable than the relaxed surface energy of the substrate $Cu_2O(111)$, explaining the carefully controlled experimental conditions required to prepare them. The calculated Bader charge is 0.139 e^- smaller for the exposed Cu atoms in

$CuO(\bar{1}11)/Cu_2O(111)$ than in the pristine $CuO(\bar{1}11)$ surface. However, the subsequent deposition of the thin film $TiO_2(111)$ increases the charge of the Ti atoms by only 0.024 e^- with respect to its pure surface. The formation of the binary heterojunction forces a large (modest) reduction by 0.448 (0.174) μ_B $atom^{-1}$ of the magnetic moment of the Cu (O) ions, compared to the value in the perfect $CuO(\bar{1}11)$ surface. Our simulations indicate that the magnetisation of the middle $CuO(\bar{1}11)$ thin film induces magnetic moments one order of magnitude smaller on the atoms of the $TiO_2(111)$ top thin film. The DFT modelling indicates that the deposition of the $CuO(\bar{1}11)$ layer onto the substrate raises the work function by 1.454 eV with respect to the value of this descriptor in the pristine $Cu_2O(111)$ surface. Likewise, the formation of the ternary heteroepitaxial junction leads to a further increase by 1.169 eV of the work function of the nanodevice.

3.8. Simulation of the molecular adsorption properties

We next investigated the adsorption properties of the binary and ternary layered heterojunction devices. We have considered the interaction of the single molecules probed experimentally, *i.e.* H_2, C_2H_5OH and *n*-C_4H_9OH, with the symmetrically inequivalent adsorption sites. We believe that these early molecular adsorption processes will determine the kinetics of the oxidation reactions that are discussed within the oxygen chemisorption model in the **Text S4** (Supporting Information). The O atoms from the VOC molecules were initially placed at 1.5 Å away from the closest transition metal atom of the sensing device and were subsequently optimised to their equilibrium configurations and energies. For the pristine heterostructures, the H_2 molecule was introduced interacting instead with the surface O atoms. Previous studies of nanosensor devices based on ZnO have shown that the interaction between these atoms of opposite Coulomb charges led to the most stable adsorption configurations [78,79].

Table S5 lists the adsorption energies for the binding of the VOCs and molecular hydrogen onto both the exposed Cu and O atoms, respectively, of the binary heteroepitaxial structure $CuO(\bar{1}11)/Cu_2O(111)$. The largest adsorption energy E_{ads} = −1.072 eV was calculated for C_2H_5OH, which was followed by E_{ads} = −0.833 eV for *n*-C_4H_9OH on the most reactive under-coordinated 3-fold Cu site of the binary layered device. From a thermodynamic point of view, C_2H_5OH and *n*-C_4H_9OH have a strength of binding towards the undercoordinated 3-fold Cu site which is ~0.3 and ~0.05 eV larger, respectively, than their fully coordinated planar 4-fold counterpart. Moreover, the difference is also 0.05 eV for the energy released by the H_2 molecule on the two types of O atoms. Our simulations suggest that H_2 shows the lowest preference for the binary heterostructure, which is in agreement with the low gas response reported for this gas from the experiments. We found that the incorporation of the $TiO_2(111)$ layer to the sensing device reduces the number of symmetrically inequivalent adsorption sites to one type of O atom and one type of Ti atom. The binding energy of the alcohol with the lowest (largest) molecular weight is reduced by approximately 0.22 (0.08) eV on the Ti positions of the ternary heterostructure with respect to the Cu atom of $CuO(\bar{1}11)/Cu_2O(111)$. However, the energetic preference of H_2 becomes larger by just 0.01 eV on the O site of $TiO_2(111)/CuO(\bar{1}11)/Cu_2O(111)$ compared to the exposed anion on the binary heterojunction. The decreasing order of binding strength found for the alcohols on the Ti site and for H_2 on the O position is $E_{ads}(H_2) \gg E_{ads}$(*n*-C_4H_9OH) > $E_{ads}(C_2H_5OH)$.

Figure 11 and **Figure 12** illustrate the most favourable molecular adsorption modes of H_2 and the alcohols on the surface of the binary and ternary heterojunctions, which is in agreement with previous studies [78,79]. The small H_2 molecule is adsorbed almost perpendicularly to the surface on a 3-fold O site lying in the ridge along the $[2\bar{1}\bar{1}]$ direction. This is the weakest interaction reported in this study, which is characterised by an interfacial H−O distance of 2.43 Å. H_2 was also initially placed above a 4-fold O atom in the grove along the $[2\bar{1}\bar{1}]$ direction, but it moved

outwards during optimisation. In the resulting adsorption, H_2 forms a bidentate-binuclear mode, since it lies flat to the surface spanning the gap between two opposite 3-fold O atoms in parallel ridges, as displayed in **Figure 11a**. The results from the calculations indicate that the H−O distance between H_2 and the surface is 0.14 Å larger across the 3-fold Cu side than the 4-fold Cu side. Nevertheless, the interaction with the surface led to a negligible stretching by 0.01 Å of the intra-atomic H−H distance with respect to the isolated molecule, but only for the adsorption at the groove site. We did not find evidence of H_2 dissociation in our calculations and thus, we speculate that this process is unlikely from a thermodynamic point of view. We found that the O of C_2H_5OH binds the surface 3- and 4-fold Cu atoms at 2.15 and 2.43 Å, respectively, as shown in **Figure 11a**. Given its small size, this molecule is able to place itself parallel to the surface grooves along the $[2\bar{1}\bar{1}]$ direction, by forming hydrogen bonds to the exposed 3-fold O atoms at the top of the ridge. Interestingly, we calculated the shortest distance of 1.95 Å for the interaction between the hydroxyl H and the surface O of the $[CuO_{3/2}]$ unit nearest to the coordinated 3-fold Cu. However, C_2H_5OH forms hydrogen bonds with the O belonging to the same $[CuO_{4/2}]$ unit of the coordinated 4-fold Cu atom at the largest distance of 2.02 Å. The shortest distances for the interaction of C_2H_5OH at the 3-fold Cu position explain our strongest calculated DFT adsorption energy for this site. We observed a difference of just 0.08 Å for the interfacial bond distances between the 3- and 4-fold Cu sites and the O atoms for the heavier *n*-C_4H_9OH molecule, see **Figure 11c**. Moreover, the hydrogen bond distances between the OH group and the surface 3-fold O atoms is 1.92 Å for both adsorption configurations investigated here. Unlike C_2H_5OH, the large and non-polar hydrocarbon chain of *n*-C_4H_9OH prefers to adsorb perpendicular to the surface plane for the interaction with the 3- and 4-fold Cu sites. Thus, this provides *n*-C_4H_9OH with the appropriate orientation and separation from the heterostructure to form its hydrogen bond to the surface O atom directly bound

to the coordinated Cu atom. We have rationalised the trend of the adsorption energies of the VOCs based on their interatomic distances to the surface, which are inversely proportional.

We have integrated the Bader charges, which indicate that the largest transfer of Δq = −0.119 e^- was found for the adsorption of the electron-rich H_2 molecule at the tetrahedral sp^3 dangling bond position of the ridge 3-fold O atom, as summarised in **Table S5**. Based on the large electronegative difference of $\Delta\chi_{HO}$ = 1.24 (Pauling scale) [80], this adsorption geometry promoted an effective charge transfer mechanism from the adsorbate to the surface. Surprisingly, the smallest charge transfer takes place from the surface to the bidentate binuclear H_2 in the adsorption at the groove position, since the adsorbate is not in a configuration that facilitates an appropriate orbital overlap with the exposed O atoms. **Figure 11a** illustrates that the interfacial charge transfer vanishes for this adsorption mode, with the electron-rich region located between the H atoms, similar to the filled σ_{1s}^{b2} bonding molecular orbital, and electron-depleted regions σ_{1s}^{*} representing the empty antibonding molecular orbital, all lying on the symmetry axis. Moreover, all VOC molecules lost electronic density upon adsorption onto the binary heteroepitaxial junction, with the observed values of charge flow in line with the trend of simulated adsorption energies. **Figure 11a** and **11b** displays the charge rearrangements between the OH group of the VOCs and the surface Cu and O atoms of the binary heterostructure, which is more noticeable for C_2H_5OH than for *n*-C_4H_9OH.

The incorporation of TiO_2 does not change noticeably the most stable adsorption geometries for the VOCs with respect to the binary sensor, but affects the configuration of the interaction for H_2, see **Figure 12a**. For the most stable adsorption, we found that H_2 prefers to sit perpendicularly to the TiO_2(111) layer at 2.56 Å above any of the quasi-equivalent O atoms. H_2 is only able to coordinate a single anion, since this surface does not form grooves with under-coordinated O atoms at the top of the ridges that allow the flat bidentate binuclear adsorption of

the molecule. **Figure 12b** illustrates that C_2H_5OH also coordinates an exposed Ti ion *via* its hydroxyl O atom, but the molecule adsorbs 0.09 Å further away from the surface site than in the case of $CuO(\bar{1}11)/Cu_2O(111)$. Given the close proximity of the surface Ti and O atoms, C_2H_5OH cannot form a strong interfacial hydrogen bond, with the H···O distance stretched to the atypical value of 2.30 Å. *n*-C_4H_9OH also forms a more detached adsorption mode on the surface of $TiO_2(111)/CuO(\bar{1}11)/Cu_2O(111)$ than in the binary device, which even prevents the formation of a hydrogen bond with the exposed O atoms, as shown in **Figure 12c**. We found that the computed charge transfers between the adsorbates and the ternary device explain their adsorption energy values, see **Table S5**. For example, the charge transfer is almost *nil* for H_2, suggesting physisorption and in agreement with its lowest adsorption energies, whereas the VOC molecules donate electron density to the surface in agreement with the strength of their adsorptions. The charge transfers for the VOCs are also smaller for the ternary device than for the binary heterostructure, which compares well and explains their relative adsorption energy values. **Figure 12a** shows the intramolecular charge redistribution resembling the molecular orbitals of H_2, with a negligible influence of the surface of the sensor. The Ti ion coordinating the OH group of C_2H_5OH loses some electronic density charge, whereas the cation coordinating the O atom of *n*-C_4H_9OH is the least perturbated for any VOC molecule, see **Figure 12b** and **12c**.

We have provided strong evidence that the change in sensitivity is the consequence of applying a layer of $TiO_2(111)$ to the $CuO(\bar{1}11)/Cu_2O(111)$ sensing device. Our DFT calculations show that the ternary heteroepitaxial junction displays smaller adsorption energies towards the VOCs than the binary nanodevice, which agrees with the gas response experiments discussed in section 3.4. We have rationalised the different behaviour of the $CuO(\bar{1}11)/Cu_2O(111)$ and $TiO_2(111)/CuO(\bar{1}11)/Cu_2O(111)$ heterojunctions based on their atomic charges and surface structures. The Bader charges calculated for both $q_{Ti} = +2.235\ e^-$ and $q_O = -1.130\ e^-$ in the ternary

device are larger than q_{Cu} = +0.867 e^- and q_O = −0.965e^- in the binary heterostructure. This supports a stronger Coulombic attraction between an equally spaced OH group of the VOCs and the surface of TiO_2(111)/CuO($\bar{1}$11)/Cu_2O(111) than the facet of the binary material. On the other hand, the separation of 3.29 Å between the exposed Cu and O atoms in neighbouring [$CuO_{3/2}$] units allows the efficient formation of both coordinate and hydrogen bonds between the CuO($\bar{1}$11)/Cu_2O(111) heteroepitaxial material and the OH group of the VOCs. However, the relative position and 1.90 Å separation between the surface counterions prevents the simultaneous formation of the Ti−OH and OH···O bonds between the adsorbate molecule and the TiO_2(111)/CuO($\bar{1}$11)/Cu_2O(111) heterojunction. Our DFT simulations suggest that the alcohols show a larger preference towards formation of the Ti−OH coordinate bond instead of the hydrogen bond with the ternary heterostructure, given the larger Coulombic attraction of the former type of interaction compared to the latter one. Moreover, the modelling indicates that the surface structure and relative position of the atoms plays a more important role than the Bader charges in determining the geometries and energies for the adsorption of the VOCs. The non-polar H_2 is the only molecule that shows both a physisorbed mode on the CuO($\bar{1}$11)/Cu_2O(111) sensor with larger adsorption energy than the chemisorbed configuration. Although the least favourable of all adsorbates explored here, H_2 is also the only molecule that displays a slightly larger adsorption energy for its physisorption mode on the ternary than on the binary device. Thus, the calculations that we have carried out offer an additional and complementary understanding, from a molecular point of view, into the sensing mechanism of the binary and ternary heteroepitaxial junctions.

4. Conclusions

In this paper we have studied the heterostructure of mixed titania/cuprite/cupric oxide ($TiO_2/CuO/Cu_2O$) phases obtained *via* a facile, cost-effective, simple and reliable spray-

sputtering-annealing approach. The investigated mixed oxide semiconductor phases are nanocrystalline and possess direct optical band gaps that are preferred for sensing applications, owing to direct recombination with the release of the energy. We have discussed the material properties and enhanced gas detecting characteristics of the CuO/Cu_2O nanolayered heterojunction device structure based on two precise phases, i.e. CuO and Cu_2O. The effect of the different thicknesses on the sensor performances is reported for the Cu_2O/CuO nanolayered crystalline heterojunction as well. The method presented in this work allows for the preparation of high-quality nanomaterials with different compositions and crystal phases. CuO/Cu_2O nano-layers with a thickness between 20 and 30 nm, which were prepared using conventional thermal annealing at 420°C for 0.5 h, stand out having promising sensing characteristics in terms of good selectivity and high response to volatile organic compounds. The best results, with a response of about 150% to 100 ppm of ethanol were achieved at a working temperature of 350°C.

The CuO/Cu_2O samples show a high selectivity and response to ethanol, which improved, alongside the long-term stability of the sensor, after surface coverage with a thin layer of TiO_2 titania. We also noted that, even after the deposition of titanium oxide, the response to ethanol did not change significantly. In general, *p-type* semiconducting oxides, such as CuO/Cu_2O, will allow a complete reaction of ethanol, which will result in increasing sensing performances to its vapors. Also, we found that the response to ethanol vapors has bisected for the CuO/Cu_2O samples, whereas it remained unchanged in the case of the $TiO_2/CuO/Cu_2O$ samples significant changes were not observed due to the self-cleaning effect of the ternary heterostructure [55,56]. These results provide evidence that the deposited thin TiO_2 film protects the sensor, increasing its lifespan. Thus, the titania (TiO_2) ultra-thin layers deposited on top of Cu_2O/CuO using spray pyrolysis method can be used for long-term stabilization of functionalities of sensors to provide protection against corrosion at high temperatures [27–30,55,56]

We have used first-principle techniques to simulate the formation of the binary $CuO(\bar{1}11)/Cu_2O(111)$ and ternary $TiO_2(111)/CuO(\bar{1}11)/Cu_2O(111)$ heterostructures, as well as their reactivity towards H_2, C_2H_5OH and *n*-C_4H_9OH. We have investigated the deposition of the monoclinic $CuO(\bar{1}11)$ and $TiO_2(111)$ thin film overlayers on the $Cu_2O(111)$ surface substrate with hexagonal symmetry and found that despite the lattice mismatch, these are thermodynamically stable systems. The binary and ternary heterostructures are thermodynamically stable. The value of the work function rises with the number of components of the heterojunctions, which is consistent with their different sensitivities. The study of the affinity of the VOCs and H_2 towards the binary and ternary heterostructures shows that the adsorbates interact molecularly with the surface of the sensors. H_2 and C_2H_5OH release the smallest and largest adsorption energy in their ground state interaction configurations, respectively, on the surfaces of both nanodevices in agreement with their similar selectivity. The electronic properties of the ground state adsorption configurations alongside the surface structure are important descriptors that explain the trends of binding energies.

■ ASSOCIATED CONTENT

Supporting Information: Details on the surface properties of the binary and ternary heteroepitaxial interfaces simulated using DFT calculations as implemented within the VASP. Cross-section view of set #1 devices made from nanolayers of CuO/Cu_2O (Device 1), and sets #2 based on $TiO_2/CuO/Cu_2O$ heterolayers (Device 2) are presented. Micro-Raman spectra of ultra-thin crystallite films of CuO/Cu_2O and of $TiO_2/CuO/Cu_2O$ thermal annealed at 420°C in air with five different thicknesses are shown, respectively. Comparison of Micro-Raman spectra for CuO/Cu_2O with $TiO_2/CuO/Cu_2O$ thermal annealed at 420°C for 30 min in air is mentioned. The cuprite oxide (Cu_2O) lattice in simple cubic according to the translational group it is described by

over-all cubic symmetry. The zone centre normal modes for TiO_2, CuO and Cu_2O are explained. Transmission spectra of $TiO_2/CuO/Cu_2O$ heterostructure and plot of absorption near the UV edge vs. wavelength for same heterostructures are shown. Plot the $(\alpha h\nu)^2$ *vs*. photon energy hν for CuO/Cu_2O, $TiO_2/CuO/Cu_2O$ heterostructure is reported. Dynamic response to 1 ppm concentration of ethanol for CuO/Cu_2O and $TiO_2/CuO/Cu_2O$ samples with thicknesses of 20 nm (Cu20) and 30 nm (Cu30). Dynamic response at different concentration of ethanol for CuO/Cu_2O (Cu20) samples, $TiO_2/CuO/Cu_2O$ (Cu20) samples, CuO/Cu_2O (Cu30) samples and $TiO_2/CuO/Cu_2O$ (Cu30) samples. Gas response at different concentration of hydrogen versus the type of samples for CuO/Cu_2O samples and $TiO_2/CuO/Cu_2O$ samples with different thicknesses of 20 nm (Cu20), 30 nm (Cu30), 40 nm (Cu40), 50 nm (Cu50) and 60 nm (Cu60), respectively, measured at 350 ^oC. The sensing mechanism is proposed. Energy band diagrams of heterostructures $TiO_2/CuO/Cu_2O$ in air and in ethanol vapors are ilustrated. Calculated unit cell lattice parameters (*a*, *b* and *c*), atomic charges (*q*), atomic magnetic moments (*m*) and band gap energy (E_g) for the cubic cuprite Cu_2O, monoclinic tenorite CuO and tetragonal anatase TiO_2. Calculated staggering parameter *y* and angle β are reported for CuO. Oxidation state (OS) and experimental values for *a*, *b*, *c*, *y*, β, *m* and E_g are indicated for all phases. The calculated Bader charges are displayed. Side (top panels) and top (bottom panels) views of the optimised structures for terminations (a) *A* and (b) *B* of the $Cu_2O(111)$ surface. Crystallographic directions and stacking sequence of the atomic layers are indicated. Side (top panels) and top (bottom panels) views of the optimised structures for terminations (a) *A* and (b) *B* of the $CuO(\bar{1}11)$ surface. Crystallographic directions and stacking sequence of the atomic layers are indicated. Side (top panel) and top (bottom panel) views of the optimised structures of the $TiO_2(111)$ surface, crystallographic directions and stacking sequence of the atomic layers are indicatedSurface energies before (γ_u) and after relaxation (γ_r) and the percentage of relaxation (*R*) for terminations *A* and *B* of the pristine

$Cu_2O(111)$, $CuO(\bar{1}11)$ and $TiO_2(111)$ surfaces. The average atomic charges (q), average magnetic moments (m) and work function (Φ), are also indicated for each surface. Geometric misfit parameter (ζ) and interfacial free energy (σ_{int}) for $CuO(\bar{1}11)$ on $Cu_2O(111)$ and $TiO_2(111)$ on $CuO(\bar{1}11)/Cu_2O(111)$. The average atomic charges (q), average magnetic moments (m) and work function (Φ), are also indicated for each surface. Adsorption energies (E_{ads}) and charge transfers (Δq) for H_2, C_2H_5OH and n-C_4H_9OH on the heterostructures $CuO(\bar{1}11)/Cu_2O(111)$ and $TiO_2(111)/CuO(\bar{1}11)/Cu_2O(111)$. The adsorption site of the adsorbate on the surface of the heterostructures is also indicated. A negative value of Δq denote that the adsorbate loses electronic charge. Response to 100 ppm of ethanol versus operating temperature of the samples CuO/Cu_2O and $TiO_2/CuO/Cu_2O$ with different thicknesses of 20 nm (Cu20), 40 nm (Cu40), 50 nm (Cu50) and 60 nm (Cu60), respectively. Response to 100 ppm of hydrogen versus operating temperature of the samples CuO/Cu_2O and $TiO_2/CuO/Cu_2O$ with different thicknesses of 20 nm (Cu20), 40 nm (Cu40), 50 nm (Cu50) and 60 nm (Cu60), respectively. Response to different gases (hydrogen, *n*-butanol, 2-propanol, ethanol, acetone and ammonia) versus operating temperature of $TiO_2/CuO/Cu_2O$ sample set with thickness of 30 nm (Cu30) and dynamic response to 2-Propanol of $TiO_2/CuO/Cu_2O$ sample set with thickness of 30 nm (Cu30) to different operating temperature. Response to different gases (hydrogen, *n*-butanol, 2-propanol, ethanol, acetone and ammonia) versus applied voltage of $TiO_2/CuO/Cu_2O$ samples with thickness of 20 nm (Cu20). Response to different gases (hydrogen, *n*-butanol, 2-propanol, ethanol, acetone and ammonia) versus applied voltage of $TiO_2/CuO/Cu_2O$ samples with thickness of 30 nm (Cu30). Dynamic response to *n*-butanol of $TiO_2/CuO/Cu_2O$ sample set with thickness of 20 nm (Cu20). SEM images of the $TiO_2/CuO/Cu_2O$ samples at lower magnification with different thickness of 20 nm and 40 nm. The Supporting Information is available free of charge on the ACS Publications website at http://pubs.acs.org

Cite this paper as : O. Lupan, D. Santos-Carballal, N. Ababii, N. Magariu, S. Hansen, A. Vahl, L. Zimoch, M. Hoppe, T. Pauporté, V. Galstyan, V. Sontea, L. Chow, N. H de Leeuw, F. Faupel, R. Adelung, E. Comini, $TiO_2/Cu_2O/CuO$ Multi-nanolayers as Sensors for H_2 and VOCs: An Experimental and Theoretical Investigation.
ACS Appl. Mater. Interfaces 13 (2021) 32363–32380.

■ AUTHOR INFORMATION

Corresponding Authors
*E-mails: ollu@tf.uni-kiel.de, oleg.lupan@mib.utm.md (O.L.); ra@tf.uni-kiel.de (R.A.); ff@tf.uni-kiel.de (F.F.); sn@tf.uni-kiel.de (S.N.); d.santos-carballal@leeds.ac.uk (D.S.C.);

Notes
The authors declare no competing interest.

AUTHOR CONTRIBUTIONS

O.L., N.A., M.H., and L.Z. have synthesized the $CuO/Cu_2O/Cu$ nanomaterials and developed the synthesis methodology. A.V. and F.F. performed all XPS investigations, analyzed the XPS results and drafted part for the article. O.L., N.A., E.C., V.G. and S.N. fitted a technological procedure for micro-nanomaterial integration into the devices for detecting VOC. N.A., V.G., E.C. and O.L. realized the measurement of the detecting characteristics of the $CuO/Cu_2O/Cu$ materials, analyzed the data and drafted part for the article. Th.P. and O.L. performed the optical measurements. Th.P. performed the titania deposition. O.L., D.S.-C., N.A., A.V., E.C., N.H.d.L., R.A., V.G. and S.H. analyzed the data from experiments and worked on the manuscript. D.S.-C. and N.H.d.L. carried out the DFT simulations and drafted computational part for the article. O.L., R.A., E.C., F.F., N.A., L.C., S.N., N.H.d.L. and D.S.-C. conceived and designed the study and gave the final approval of the draft to be submitted and to be published. O.L., E.C., L.C. and R.A. performed the design and conception for the studies, and approval. The work was written based on contributions by all authors, who all reviewed the manuscript.

FUNDING

Cite this paper as : O. Lupan, D. Santos-Carballal, N. Ababii, N. Magariu, S. Hansen, A. Vahl, L. Zimoch, M. Hoppe, T. Pauporté, V. Galstyan, V. Sontea, L. Chow, N. H de Leeuw, F. Faupel, R. Adelung, E. Comini, $TiO_2/Cu_2O/CuO$ Multi-nanolayers as Sensors for H_2 and VOCs: An Experimental and Theoretical Investigation.
ACS Appl. Mater. Interfaces 13 (2021) 32363–32380.
Federal Ministry of Education and Research by the project “PorSSi” (03XP0126 B) and the EKSH for supporting this research by “3D strukturierte Kohlenstoff-Schwefel Gerüstmaterialien als neuartiges und nachhaltiges Kathodenmaterial für Hochenergie Lithium-Ionen Akkus”.

German Research Foundation (DFG- Deutsche Forschungsgemeinschaft) under the schemes SFB1261, FOR2093 & AD 183/16-1 and by Project SFB859.

NATO Science for Peace and Security Programme (SPS) within the grant G5634 „Advanced Electro-Optical Chemical Sensors” AMOXES.

Additionally, the authors thank the WTSH and the EUSH for partially funding this project BAEW with (LPW-E/1.1.2/1486).

ACKNOWLEDGMENTS

This research was sponsored in part by the NATO Science for Peace and Security Programme (SPS) within the grant G5634 „Advanced Electro-Optical Chemical Sensors” AMOXES. Dr. Lupan gratefully acknowledges PSL University, Chimie-ParisTech for an invited position as professor in 2018 and 2019. This research was sponsored partially by the German Research Foundation (DFG- Deutsche Forschungsgemeinschaft) under the schemes PAK 902 (SFB1261, FOR2093 & AD 183/16-1) and by Project SFB859. This work was financially supported by the German Research Foundation (DFG) via the research unit FOR 2093 "Memristive devices for neuronal systems" through project A2. The Federal Ministry of Education and Research through the project “PorSSi” (03XP0126 B) and the EKSH also supported this research by “3D strukturierte Kohlenstoff-Schwefel Gerüstmaterialien als neuartiges und nachhaltiges Kathodenmaterial für Hochenergie Lithium-Ionen Akkus”. Additionally, the authors thank the WTSH and the EUSH for partially funding this project BAEW with (LPW-E/1.1.2/1486).

Cite this paper as : O. Lupan, D. Santos-Carballal, N. Ababii, N. Magariu, S. Hansen, A. Vahl, L. Zimoch, M. Hoppe, T. Pauporté, V. Galstyan, V. Sontea, L. Chow, N. H de Leeuw, F. Faupel, R. Adelung, E. Comini, $TiO_2/Cu_2O/CuO$ Multi-nanolayers as Sensors for H_2 and VOCs: An Experimental and Theoretical Investigation.
ACS Appl. Mater. Interfaces 13 (2021) 32363–32380.
Via our membership of the UK's HEC Materials Chemistry Consortium, which is funded by EPSRC (EP/L000202, and EP/R029431), this work used the ARCHER UK National Supercomputing Service (http://www.archer.ac.uk). This work was undertaken on ARC4, part of the High-Performance Computing facilities at the University of Leeds, United Kingdom. All data is provided in full in the Results and Discussion section of this paper.

■ References

(1) Hoppe, M.; Ababii, N.; Postica, V.; Lupan, O.; Polonskyi, O.; Schütt, F.; Kaps, S.; Sukhodub, L. F.; Sontea, V.; Strunskus, T.; Faupel, F.; Adelung, R. ($CuO-Cu_2O$)/ZnO:Al Heterojunctions for Volatile Organic Compound Detection. *Sensors Actuators B Chem.* **2018**, *255*, 1362–1375.

(2) Zappa, D.; Galstyan, V.; Kaur, N.; Munasinghe Arachchige, H. M. M.; Sisman, O.; Comini, E. "Metal Oxide -Based Heterostructures for Gas Sensors"- A Review. *Anal. Chim. Acta* **2018**, *1039*, 1–23.

(3) Su, C.; Zhang, L.; Han, Y.; Ren, C.; Li, B.; Wang, T.; Zeng, M.; Su, Y.; Hu, N.; Zhou, Z.; Wang, Y.; Yang, Z.; Xu, L. Glucose-Assisted Synthesis of Hierarchical NiO-ZnO Heterostructure with Enhanced Glycol Gas Sensing Performance. *Sensors Actuators B Chem.* **2021**, *329*, 129167.

(4) Nordseth, Ø.; Kumar, R.; Bergum, K.; Fara, L.; Dumitru, C.; Craciunescu, D.; Dragan, F.; Chilibon, I.; Monakhov, E.; Foss, S.; Svensson, B. Metal Oxide Thin-Film Heterojunctions for Photovoltaic Applications. *Materials (Basel).* **2018**, *11* (12), 2593.

(5) Wu, E.; Xie, Y.; Yuan, B.; Zhang, H.; Hu, X.; Liu, J.; Zhang, D. Ultrasensitive and Fully Reversible NO_2 Gas Sensing Based on P-Type $MoTe_2$ under Ultraviolet Illumination. *ACS Sensors* **2018**, *3* (9), 1719–1726.

(6) Lupan, O.; Cretu, V.; Postica, V.; Polonskyi, O.; Ababii, N.; Schütt, F.; Kaidas, V.; Faupel, F.; Adelung, R. Non-Planar Nanoscale p–p Heterojunctions Formation in $Zn_xCu_{1-x}O_y$ Nanocrystals by Mixed Phases for Enhanced Sensors. *Sensors Actuators B Chem.* **2016**, *230*, 832–843.

(7) Brattain, W. H.; Bardeen, J. Surface Properties of Germanium. *Bell Syst. Tech. J.* **1953**, *32* (1), 1–41.

(8) McWilliams, S.; Flynn, C. D.; McWilliams, J.; Arnold, D. C.; Wahyuono, R. A.; Undisz, A.; Rettenmayr, M.; Ignaszak, A. Nanostructured Cu_2O Synthesized via Bipolar Electrochemistry. *Nanomaterials* **2019**, *9* (12), 1781.

(9) Verma, N.; Kumar, N. Synthesis and Biomedical Applications of Copper Oxide Nanoparticles: An Expanding Horizon. *ACS Biomater. Sci. Eng.* **2019**, *5* (3), 1170–1188.

(10) Brattain, W. H. The Copper Oxide Rectifier. *Rev. Mod. Phys.* **1951**, *23* (3), 203–212.

(11) Lupan, O.; Postica, V.; Cretu, V.; Wolff, N.; Duppel, V.; Kienle, L.; Adelung, R. Single and Networked CuO Nanowires for Highly Sensitive P-Type Semiconductor Gas Sensor Applications. *Phys. status solidi - Rapid Res. Lett.* **2016**, *10* (3), 260–266.

(12) Tiginyanu, I. M.; Lupan, O.; Ursaki, V. V.; Chow, L.; Enachi, M. Nanostructures of Metal Oxides. In *Comprehensive Semiconductor Science and Technology*; Bhattacharya, P., Fornari, R., Kamimura, H., Eds.; Elsevier: Amsterdam, **2011**; pp 396–479.

(13) Bendavid, L. I.; Carter, E. A. First-Principles Predictions of the Structure, Stability, and Photocatalytic Potential of Cu_2O Surfaces. *J. Phys. Chem. B* **2013**, *117* (49), 15750–15760.

(14) Siebert, L.; Lupan, O.; Mirabelli, M.; Ababii, N.; Terasa, M.-I.; Kaps, S.; Cretu, V.; Vahl, A.; Faupel, F.; Adelung, R. 3D-Printed Chemiresistive Sensor Array on Nanowire $CuO/Cu_2O/Cu$

Heterojunction Nets. *ACS Appl. Mater. Interfaces* **2019**, *11* (28), 25508–25515.

(15) Vahl, A.; Carstensen, J.; Kaps, S.; Lupan, O.; Strunskus, T.; Adelung, R.; Faupel, F. Concept and Modelling of Memsensors as Two Terminal Devices with Enhanced Capabilities in Neuromorphic Engineering. *Sci. Rep.* **2019**, *9* (1), 4361.

(16) Steinhauer, S. Gas Sensors Based on Copper Oxide Nanomaterials: A Review. *Chemosensors* **2021**, *9* (3), 51.

(17) Moseley, P. T. Progress in the Development of Semiconducting Metal Oxide Gas Sensors: A Review. *Meas. Sci. Technol.* **2017**, *28* (8), 082001.

(18) Kim, H.-J.; Lee, J.-H. Highly Sensitive and Selective Gas Sensors Using P-Type Oxide Semiconductors: Overview. *Sensors Actuators B Chem.* **2014**, *192*, 607–627.

(19) Degler, D.; Weimar, U.; Barsan, N. Current Understanding of the Fundamental Mechanisms of Doped and Loaded Semiconducting Metal-Oxide-Based Gas Sensing Materials. *ACS Sensors* **2019**, *4* (9), 2228–2249.

(20) Saruhan, B.; Lontio Fomekong, R.; Nahirniak, S. Review: Influences of Semiconductor Metal Oxide Properties on Gas Sensing Characteristics. *Front. Sensors* **2021**, *2*, 2.

(21) Mishra, A. K.; Roldan, A.; de Leeuw, N. H. A Density Functional Theory Study of the Adsorption Behaviour of CO_2 on Cu_2O Surfaces. *J. Chem. Phys.* **2016**, *145* (4), 044709.

(22) Siegfried, M. J.; Choi, K.-S. Elucidating the Effect of Additives on the Growth and Stability of Cu_2O Surfaces via Shape Transformation of Pre-Grown Crystals. *J. Am. Chem. Soc.* **2006**, *128* (32), 10356–10357.

(23) Mishra, A. K.; Roldan, A.; de Leeuw, N. H. CuO Surfaces and CO_2 Activation: A Dispersion-Corrected DFT+ U Study. *J. Phys. Chem. C* **2016**, *120* (4), 2198–2214.

(24) Du, Y. E.; Feng, Q.; Chen, C.; Tanaka, Y.; Yang, X. Photocatalytic and Dye-Sensitized Solar Cell Performances of {010}- Faceted and [111]-Faceted Anatase TiO_2 Nanocrystals Synthesized from Tetratitanate Nanoribbons. *ACS Appl. Mater. Interfaces* **2014**, *6* (18), 16007–16019.

(25) Xu, H.; Reunchan, P.; Ouyang, S.; Tong, H.; Umezawa, N.; Kako, T.; Ye, J. Anatase TiO_2 Single Crystals Exposed with High-Reactive {111} Facets toward Efficient H_2 Evolution. *Chem. Mater.* **2013**, *25* (3), 405–411.

(26) Popov, A. P.; Priezzhev, A. V; Lademann, J.; Myllylä, R. TiO_2 Nanoparticles as an Effective UV-B Radiation Skin-Protective Compound in Sunscreens. *J. Phys. D. Appl. Phys.* **2005**, *38* (15), 2564–2570.

(27) Veziroglu, S.; Hwang, J.; Drewes, J.; Barg, I.; Shondo, J.; Strunskus, T.; Polonskyi, O.; Faupel, F.; Aktas, O. C. PdO Nanoparticles Decorated TiO_2 Film with Enhanced Photocatalytic and Self-Cleaning Properties. *Mater. Today Chem.* **2020**, *16*, 100251.

(28) Abdeen, D.; El Hachach, M.; Koc, M.; Atieh, M. A Review on the Corrosion Behaviour of Nanocoatings on Metallic Substrates. *Materials (Basel).* **2019**, *12* (2), 210.

(29) Boukerche, S.; Himour, A.; Bououdina, M.; Bensouici, F.; Ouchenane, S. Multilayered ZnO/TiO_2 Nanostructures as Efficient Corrosion Protection for Stainless Steel 304. *Mater. Res. Express* **2019**, *6* (5), 055052.

(30) Won, Y.; Schwartzenberg, K.; Gray, K. A. TiO_2-Based Transparent Coatings Create Self-Cleaning Surfaces. *Chemosphere* **2018**, *208*, 899–906.

(31) Zeng, G.; Wu, C.; Chang, Y.; Zhou, C.; Chen, B.; Zhang, M.; Li, J.; Duan, X.; Yang, Q.; Pang, W. Detection and Discrimination of Volatile Organic Compounds Using a Single Film Bulk Acoustic Wave Resonator with Temperature Modulation as a Multiparameter Virtual Sensor Array. *ACS Sensors* **2019**, *4* (6), 1524–1533.

(32) Righettoni, M.; Tricoli, A. Toward Portable Breath Acetone Analysis for Diabetes Detection. *J. Breath Res.* **2011**, *5* (3), 037109.

(33) Siebert, L.; Wolff, N.; Ababii, N.; Terasa, M.-I.; Lupan, O.; Vahl, A.; Duppel, V.; Qiu, H.; Tienken, M.; Mirabelli, M.; Sontea, V.; Faupel, F.; Kienle, L.; Adelung, R. Facile Fabrication of Semiconducting Oxide Nanostructures by Direct Ink Writing of Readily Available Metal

Microparticles and Their Application as Low Power Acetone Gas Sensors. *Nano Energy* **2020**, *70*, 104420.

(34) Tassopoulos, C. N.; Barnett, D.; Russell Fraser, T. Breath-Acetone and Blood-Sugar Measurements in Diabetes. *Lancet* **1969**, *293* (7609), 1282–1286.

(35) Galstyan, V.; Poli, N.; D'Arco, A.; Macis, S.; Lupi, S.; Comini, E. A Novel Approach for Green Synthesis of WO_3 Nanomaterials and Their Highly Selective Chemical Sensing Properties. *J. Mater. Chem. A* **2020**, *8* (39), 20373–20385.

(36) Hakim, M.; Broza, Y. Y.; Barash, O.; Peled, N.; Phillips, M.; Amann, A.; Haick, H. Volatile Organic Compounds of Lung Cancer and Possible Biochemical Pathways. *Chem. Rev.* **2012**, *112* (11), 5949–5966.

(37) Adiguzel, Y.; Kulah, H. Breath Sensors for Lung Cancer Diagnosis. *Biosens. Bioelectron.* **2015**, *65*, 121–138.

(38) Suematsu, K.; Harano, W.; Oyama, T.; Shin, Y.; Watanabe, K.; Shimanoe, K. Pulse-Driven Semiconductor Gas Sensors Toward Ppt Level Toluene Detection. *Anal. Chem.* **2018**, *90* (19), 11219–11223.

(39) Krilaviciute, A.; Heiss, J. A.; Leja, M.; Kupcinskas, J.; Haick, H.; Brenner, H. Detection of Cancer through Exhaled Breath: A Systematic Review. *Oncotarget* **2015**, *6* (36), 38643–38657.

(40) Amann, A.; Mochalski, P.; Ruzsanyi, V.; Broza, Y. Y.; Haick, H. Assessment of the Exhalation Kinetics of Volatile Cancer Biomarkers Based on Their Physicochemical Properties. *J. Breath Res.* **2014**, *8* (1), 016003.

(41) Haick, H.; Broza, Y. Y.; Mochalski, P.; Ruzsanyi, V.; Amann, A. Assessment, Origin, and Implementation of Breath Volatile Cancer Markers. *Chem. Soc. Rev.* **2014**, *43* (5), 1423–1449.

(42) Ababii, N.; Hoppe, M.; Shree, S.; Vahl, A.; Ulfa, M.; Pauporté, T.; Viana, B.; Cretu, V.; Magariu, N.; Postica, V.; Sontea, V.; Terasa, M.-I.; Polonskyi, O.; Faupel, F.; Adelung, R.; Lupan, O. Effect of Noble Metal Functionalization and Film Thickness on Sensing Properties of Sprayed TiO_2 Ultra-Thin Films. *Sensors Actuators A Phys.* **2019**, *293*, 242–258.

(43) Lupan, O.; Cretu, V.; Postica, V.; Ababii, N.; Polonskyi, O.; Kaidas, V.; Schütt, F.; Mishra, Y. K.; Monaico, E.; Tiginyanu, I.; Sontea, V.; Strunskus, T.; Faupel, F.; Adelung, R. Enhanced Ethanol Vapour Sensing Performances of Copper Oxide Nanocrystals with Mixed Phases. *Sensors Actuators B Chem.* **2016**, *224*, 434–448.

(44) Wang, P.; Shao, Z.; Ulfa, M.; Pauporté, T. Insights into the Hole Blocking Layer Effect on the Perovskite Solar Cell Performance and Impedance Response. *J. Phys. Chem. C* **2017**, *121* (17), 9131–9141.

(45) Chow, L.; Lupan, O.; Heinrich, H.; Chai, G. Self-Assembly of Densely Packed and Aligned Bilayer ZnO Nanorod Arrays. *Appl. Phys. Lett.* **2009**, *94* (16), 163105.

(46) Lupan, O.; Postica, V.; Ababii, N.; Reimer, T.; Shree, S.; Hoppe, M.; Polonskyi, O.; Sontea, V.; Chemnitz, S.; Faupel, F.; Adelung, R. Ultra-Thin TiO_2 Films by Atomic Layer Deposition and Surface Functionalization with Au Nanodots for Sensing Applications. *Mater. Sci. Semicond. Process.* **2018**, *87*, 44–53.

(47) Pauporté, T.; Lupan, O.; Zhang, J.; Tugsuz, T.; Ciofini, I.; Labat, F.; Viana, B. Low-Temperature Preparation of Ag-Doped ZnO Nanowire Arrays, DFT Study, and Application to Light-Emitting Diode. *ACS Appl. Mater. Interfaces* **2015**, *7* (22), 11871–11880.

(48) Vahl, A.; Dittmann, J.; Jetter, J.; Veziroglu, S.; Shree, S.; Ababii, N.; Lupan, O.; Aktas, O. C.; Strunskus, T.; Quandt, E.; Adelung, R.; Sharma, S. K.; Faupel, F. The Impact of O_2/Ar Ratio on Morphology and Functional Properties in Reactive Sputtering of Metal Oxide Thin Films. *Nanotechnology* **2019**, *30* (23), 235603.

(49) Cretu, V.; Postica, V.; Mishra, A. K.; Hoppe, M.; Tiginyanu, I.; Mishra, Y. K.; Chow, L.; de Leeuw, N. H.; Adelung, R.; Lupan, O. Synthesis, Characterization and DFT Studies of Zinc-Doped Copper Oxide Nanocrystals for Gas Sensing Applications. *J. Mater. Chem. A* **2016**, *4* (17), 6527–6539.

(50) Pauly, N.; Tougaard, S.; Yubero, F. Determination of the Cu 2p Primary Excitation Spectra for Cu,

Cu_2O and CuO. *Surf. Sci.* **2014**, *620*, 17–22.

(51) Moulder, J. F.; Chastain, J. *Handbook of X-Ray Photoelectron Spectroscopy: A Reference Book of Standard Spectra for Identification and Interpretation of XPS Data*, illustrate.; Jill Chastain, Ed.; Physical Electronics Division, Perkin-Elmer Corporation, **1992**.

(52) Alexander V. Naumkin, Anna Kraut-Vass, Stephen W. Gaarenstroom, C. J. P. NIST X-Ray Photoelectron Spectroscopy Database, National Institute of Standards and Technology, NIST Stand. Ref. Database Number 20. (2000) 20899. *NIST X-ray Photoelectron Spectrosc. Database, NIST Stand. Ref. Database 20, Version 4.1* **2000**, Accessed: 2018-02-08.

(53) Wilson, R.; Simion, C.; Blackman, C.; Carmalt, C.; Stanoiu, A.; Di Maggio, F.; Covington, J. The Effect of Film Thickness on the Gas Sensing Properties of Ultra-Thin TiO_2 Films Deposited by Atomic Layer Deposition. *Sensors* **2018**, *18* (3), 735.

(54) Hsu, C.-L.; Tsai, J.-Y.; Hsueh, T.-J. Ethanol Gas and Humidity Sensors of CuO/Cu_2O Composite Nanowires Based on a Cu through-Silicon via Approach. *Sensors Actuators B Chem.* **2016**, *224*, 95–102.

(55) Adachi, T.; Latthe, S. S.; Gosavi, S. W.; Roy, N.; Suzuki, N.; Ikari, H.; Kato, K.; Katsumata, K.; Nakata, K.; Furudate, M.; Inoue, T.; Kondo, T.; Yuasa, M.; Fujishima, A.; Terashima, C. Photocatalytic, Superhydrophilic, Self-Cleaning TiO_2 Coating on Cheap, Light-Weight, Flexible Polycarbonate Substrates. *Appl. Surf. Sci.* **2018**, *458*, 917–923.

(56) Banerjee, S.; Dionysiou, D. D.; Pillai, S. C. Self-Cleaning Applications of TiO_2 by Photo-Induced Hydrophilicity and Photocatalysis. *Appl. Catal. B Environ.* **2015**, *176–177*, 396–428.

(57) Barsan, N.; Schweizer-Berberich, M.; Göpel, W. Fundamental and Practical Aspects in the Design of Nanoscaled SnO_2 Gas Sensors: A Status Report. *Fresenius. J. Anal. Chem.* **1999**, *365* (4), 287–304.

(58) Foo, M. L.; Huang, Q.; Lynn, J. W.; Lee, W. L.; Klimczuk, T.; Hagemann, I. S.; Ong, N. P.; Cava, R. J. Synthesis, Structure and Physical Properties of Ru Ferrites: Ba$M$$Ru_5O_{11}$ (M=Li and Cu) and Ba$M'_2Ru_4O_{11}$ (M'=Mn, Fe and Co). *J. Solid State Chem.* **2006**, *179* (2), 563–572.

(59) Downie, L. J.; Black, C.; Ardashnikova, E. I.; Tang, C. C.; Vasiliev, A. N.; Golovanov, A. N.; Berdonosov, P. S.; Dolgikh, V. A.; Lightfoot, P. Structural Phase Transitions in the Kagome Lattice Based Materials $Cs_{2-x}Rb_xSnCu_3F_{12}$ (x = 0, 0.5, 1.0, 1.5). *CrystEngComm* **2014**, *16* (32), 7419–7425.

(60) Kliche, G.; Popovic, Z. V. Far-Infrared Spectroscopic Investigations on CuO. *Phys. Rev. B* **1990**, *42* (16), 10060–10066.

(61) Leinekugel-le-Cocq-Errien, A. Y.; Deniard, P.; Jobic, S.; Gautier, E.; Evain, M.; Aubin, V.; Bart, F. Structural Characterization of the Hollandite Host Lattice for the Confinement of Radioactive Cesium: Quantification of the Amorphous Phase Taking into Account the Incommensurate Modulated Character of the Crystallized Part. *J. Solid State Chem.* **2007**, *180* (1), 322–330.

(62) Watson, G. W.; Kelsey, E. T.; de Leeuw, N. H.; Harris, D. J.; Parker, S. C. Atomistic Simulation of Dislocations, Surfaces and Interfaces in MgO. *J. Chem. Soc. Faraday Trans.* **1996**, *92* (3), 433–438.

(63) Makov, G.; Payne, M. C. Periodic Boundary Conditions in Ab Initio Calculations. *Phys. Rev. B* **1995**, *51* (7), 4014–4022.

(64) Neugebauer, J.; Scheffler, M. Adsorbate-Substrate and Adsorbate-Adsorbate Interactions of Na and K Adlayers on Al(111). *Phys. Rev. B* **1992**, *46* (24), 16067–16080.

(65) Zakaria, S. N. A.; Hollingsworth, N.; Islam, H.; Roffey, A.; Santos-Carballal, D.; Roldan, A.; Bras, W.; Sankar, G.; Hogarth, G.; Holt, K. B.; de Leeuw, N. H. Insight into the Nature of Iron Sulfide Surfaces during the Electrochemical Hydrogen Evolution and CO_2 Reduction Reactions. *ACS Appl. Mater. Interfaces* **2018**, *10* (38), 32078–32085.

(66) Santos-Carballal, D.; Roldan, A.; Grau-Crespo, R.; de Leeuw, N. H. A DFT Study of the Structures, Stabilities and Redox Behaviour of the Major Surfaces of Magnetite Fe_3O_4. *Phys. Chem. Chem. Phys.* **2014**, *16* (39), 21082–21097.

(67) Santos-Carballal, D.; Roldan, A.; de Leeuw, N. H. Early Oxidation Processes on the Greigite Fe_3S_4(001) Surface by Water: A Density Functional Theory Study. *J. Phys. Chem. C* **2016**, *120* (16),

8616–8629.

(68) Santos-Carballal, D.; Roldan, A.; Dzade, N. Y.; de Leeuw, N. H. Reactivity of CO_2 on the Surfaces of Magnetite (Fe_3O_4), Greigite (Fe_3S_4) and Mackinawite (FeS). *Philos. Trans. R. Soc. A Math. Phys. Eng. Sci.* **2018**, *376* (2110), 20170065.

(69) Santos-Carballal, D.; Roldan, A.; De Leeuw, N. H. CO_2 Reduction to Acetic Acid on the Greigite Fe_3S_4 {111} Surface. *Faraday Discuss.* **2020**.

(70) Tasker, P. W. The Stability of Ionic Crystal Surfaces. *J. Phys. C Solid State Phys.* **1979**, *12* (22), 4977–4984.

(71) Tersoff, J.; Hamann, D. R. Theory of the Scanning Tunneling Microscope. *Phys. Rev. B* **1985**, *31* (2), 805–813.

(72) Vanpoucke, D. E. P.; Brocks, G. Formation of Pt-Induced Ge Atomic Nanowires on Pt/Ge(001): A Density Functional Theory Study. *Phys. Rev. B* **2008**, *77* (24), 241308.

(73) Shields, A. E.; Santos-Carballal, D.; de Leeuw, N. H. A Density Functional Theory Study of Uranium-Doped Thoria and Uranium Adatoms on the Major Surfaces of Thorium Dioxide. *J. Nucl. Mater.* **2016**, *473*, 99–111.

(74) Ungerer, M. J.; Santos-Carballal, D.; Cadi-Essadek, A.; van Sittert, C. G. C. E.; de Leeuw, N. H. Interaction of H_2O with the Platinum Pt (001), (011), and (111) Surfaces: A Density Functional Theory Study with Long-Range Dispersion Corrections. *J. Phys. Chem. C* **2019**, *123* (45), 27465–27476.

(75) Christensen, A.; Carter, E. A. First-Principles Characterization of a Heteroceramic Interface: ZrO_2(001) Deposited on an α-Al_2O_3(1$\bar{1}$02) Substrate. *Phys. Rev. B - Condens. Matter Mater. Phys.* **2000**, *62* (24), 16968–16983.

(76) Arya, A.; Carter, E. A. Structure, Bonding, and Adhesion at the TiC(100)/Fe(110) Interface from First Principles. *J. Chem. Phys.* **2003**, *118* (19), 8982–8996.

(77) Chen, Y.; Hong, S.; Ko, H.; Kirshner, V.; Wenisch, H.; Yao, T.; Inaba, K.; Segawa, Y. Effects of an Extremely Thin Buffer on Heteroepitaxy with Large Lattice Mismatch. *Appl. Phys. Lett.* **2001**, *78* (21), 3352–3354.

(78) Postica, V.; Vahl, A.; Strobel, J.; Santos-Carballal, D.; Lupan, O.; Cadi-Essadek, A.; De Leeuw, N. H.; Schütt, F.; Polonskyi, O.; Strunskus, T.; Baum, M.; Kienle, L.; Adelung, R.; Faupel, F. Tuning Doping and Surface Functionalization of Columnar Oxide Films for Volatile Organic Compounds Sensing: Experiments and Theory. *J. Mater. Chem. A* **2018**, *6* (46), 23669–23682.

(79) Postica, V.; Vahl, A.; Santos-Carballal, D.; Dankwort, T.; Kienle, L.; Hoppe, M.; Cadi-Essadek, A.; de Leeuw, N. H.; Terasa, M.-I.; Adelung, R.; Faupel, F.; Lupan, O. Tuning ZnO Sensors Reactivity toward Volatile Organic Compounds via Ag Doping and Nanoparticle Functionalization. *ACS Appl. Mater. Interfaces* **2019**, *11* (34), 31452–31466.

(80) Allred, A. L. Electronegativity Values from Thermochemical Data. *J. Inorg. Nucl. Chem.* **1961**, *17* (3–4), 215–221.

Cite this paper as : O. Lupan, D. Santos-Carballal, N. Ababii, N. Magariu, S. Hansen, A. Vahl, L. Zimoch, M. Hoppe, T. Pauporté, V. Galstyan, V. Sontea, L. Chow, N. H de Leeuw, F. Faupel, R. Adelung, E. Comini, $TiO_2/Cu_2O/CuO$ Multi-nanolayers as Sensors for H_2 and VOCs: An Experimental and Theoretical Investigation.
ACS Appl. Mater. Interfaces 13 (2021) 32363–32380.

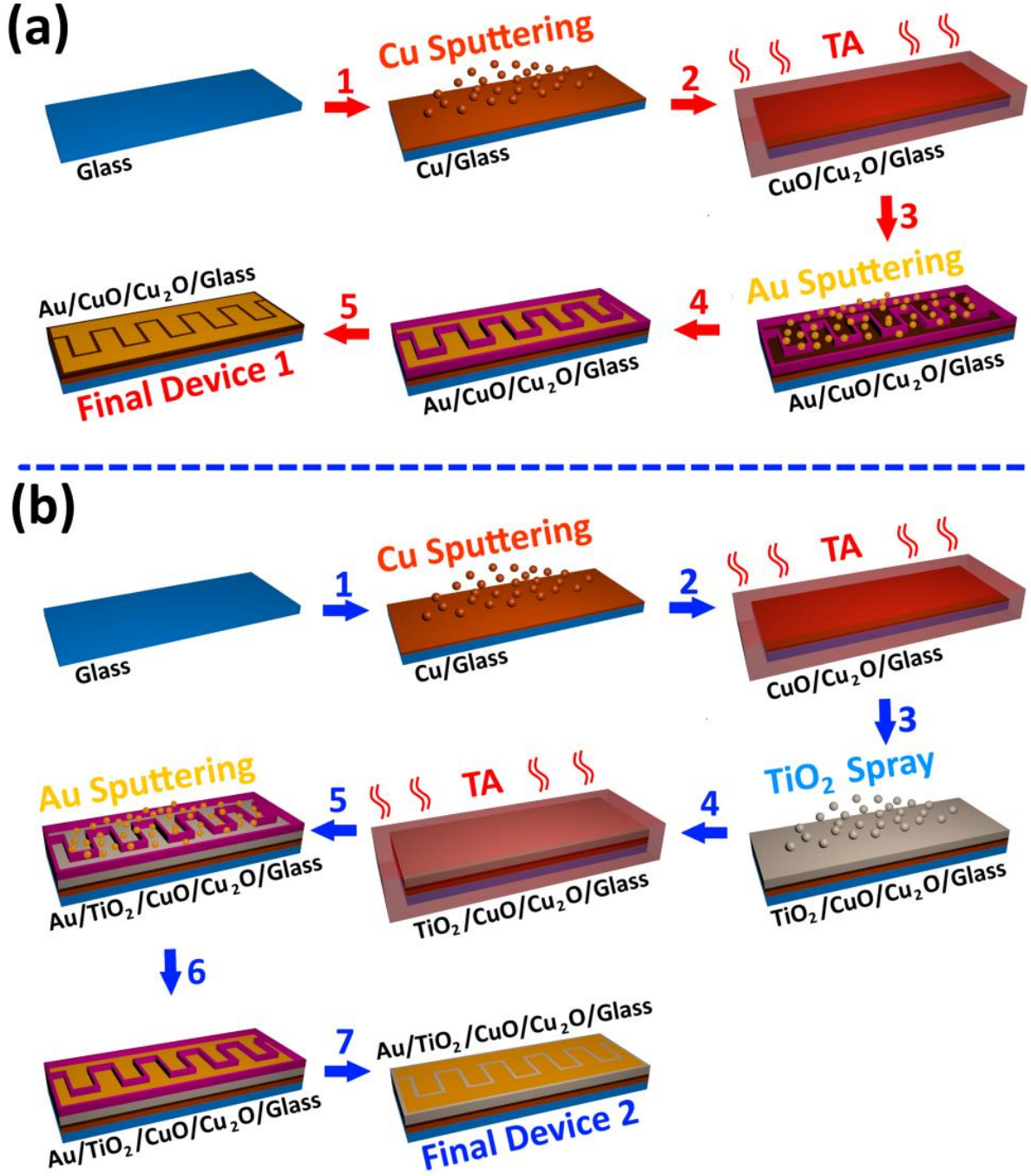

Figure 1. The technological flow chart for the manufacture of the (a) CuO/Cu_2O (Final device #1); and (b) $TiO_2/CuO/Cu_2O$ (Final device set #2) nanostructured layered films sensor devices.

Cite this paper as : O. Lupan, D. Santos-Carballal, N. Ababii, N. Magariu, S. Hansen, A. Vahl, L. Zimoch, M. Hoppe, T. Pauporté, V. Galstyan, V. Sontea, L. Chow, N. H de Leeuw, F. Faupel, R. Adelung, E. Comini, $TiO_2/Cu_2O/CuO$ Multi-nanolayers as Sensors for H_2 and VOCs: An Experimental and Theoretical Investigation.
ACS Appl. Mater. Interfaces 13 (2021) 32363–32380.

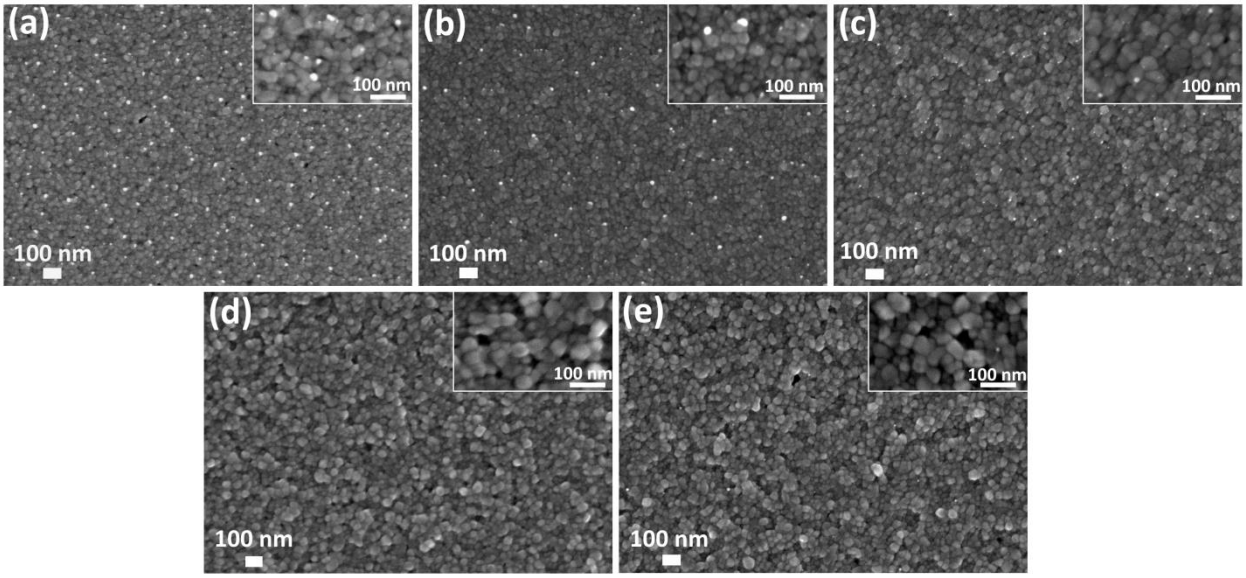

Figure 2. SEM images of the nano-crystallite CuO/Cu_2O samples grown using the sputtering-annealing approach and thermally treated at 420°C, for 30 min: (a) 20 nm; (b) 30 nm; (c) 40 nm; (d) 50 nm; and (e) 60 nm. The inset shows a higher maginification of the SEM images.

Cite this paper as : O. Lupan, D. Santos-Carballal, N. Ababii, N. Magariu, S. Hansen, A. Vahl, L. Zimoch, M. Hoppe, T. Pauporté, V. Galstyan, V. Sontea, L. Chow, N. H de Leeuw, F. Faupel, R. Adelung, E. Comini, $TiO_2/Cu_2O/CuO$ Multi-nanolayers as Sensors for H_2 and VOCs: An Experimental and Theoretical Investigation.
ACS Appl. Mater. Interfaces 13 (2021) 32363–32380.

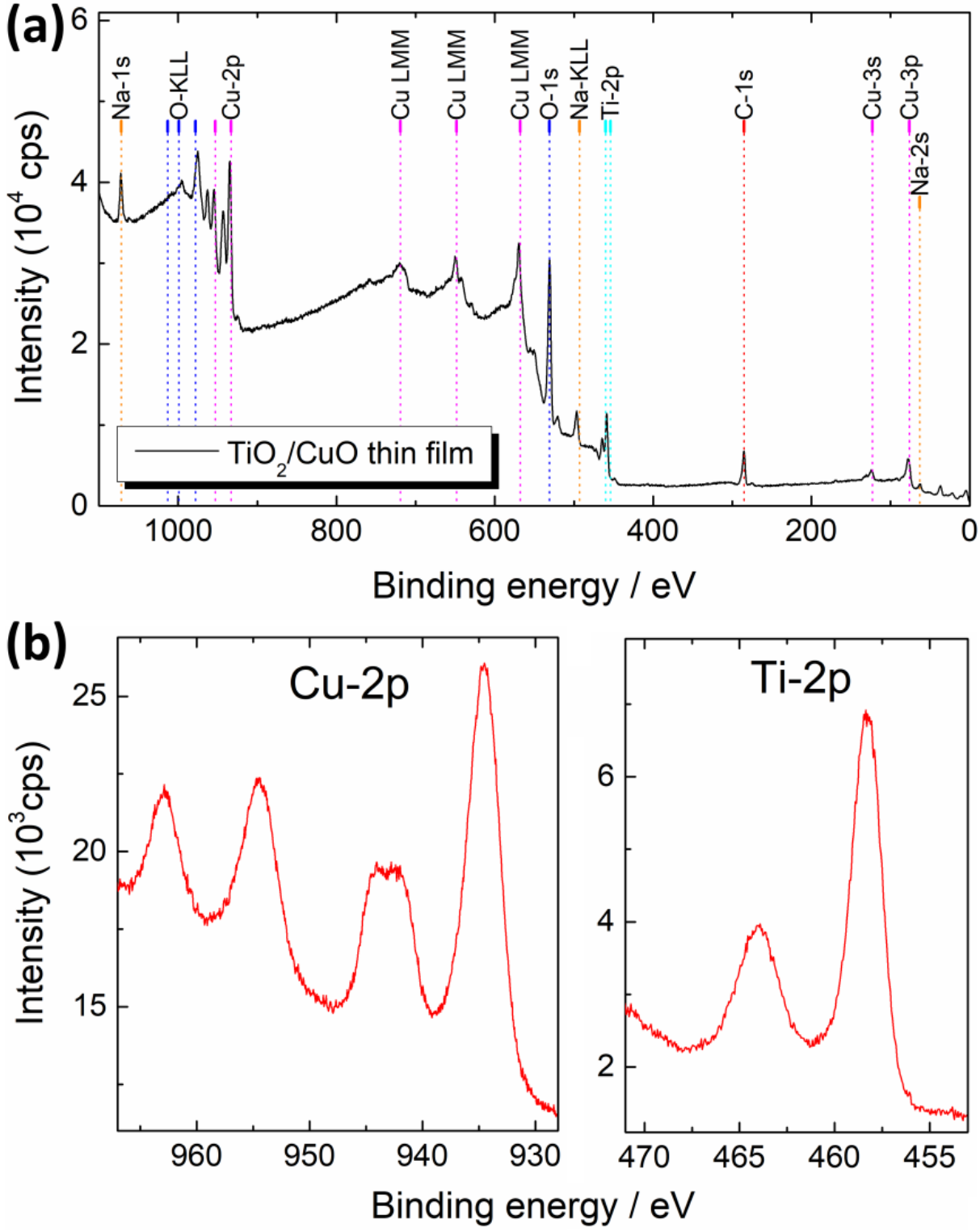

Figure 3. XPS spectra of a TiO_2-CuO (red line) thin film sensor: a) overview spectrum; b) high resolution spectra of the Cu-2p and Ti-2p lines.

Cite this paper as : O. Lupan, D. Santos-Carballal, N. Ababii, N. Magariu, S. Hansen, A. Vahl, L. Zimoch, M. Hoppe, T. Pauporté, V. Galstyan, V. Sontea, L. Chow, N. H de Leeuw, F. Faupel, R. Adelung, E. Comini, $TiO_2/Cu_2O/CuO$ Multi-nanolayers as Sensors for H_2 and VOCs: An Experimental and Theoretical Investigation.
ACS Appl. Mater. Interfaces 13 (2021) 32363–32380.

Cite this paper as : O. Lupan, D. Santos-Carballal, N. Ababii, N. Magariu, S. Hansen, A. Vahl, L. Zimoch, M. Hoppe, T. Pauporté, V. Galstyan, V. Sontea, L. Chow, N. H de Leeuw, F. Faupel, R. Adelung, E. Comini, $TiO_2/Cu_2O/CuO$ Multi-nanolayers as Sensors for H_2 and VOCs: An Experimental and Theoretical Investigation.
ACS Appl. Mater. Interfaces 13 (2021) 32363–32380.

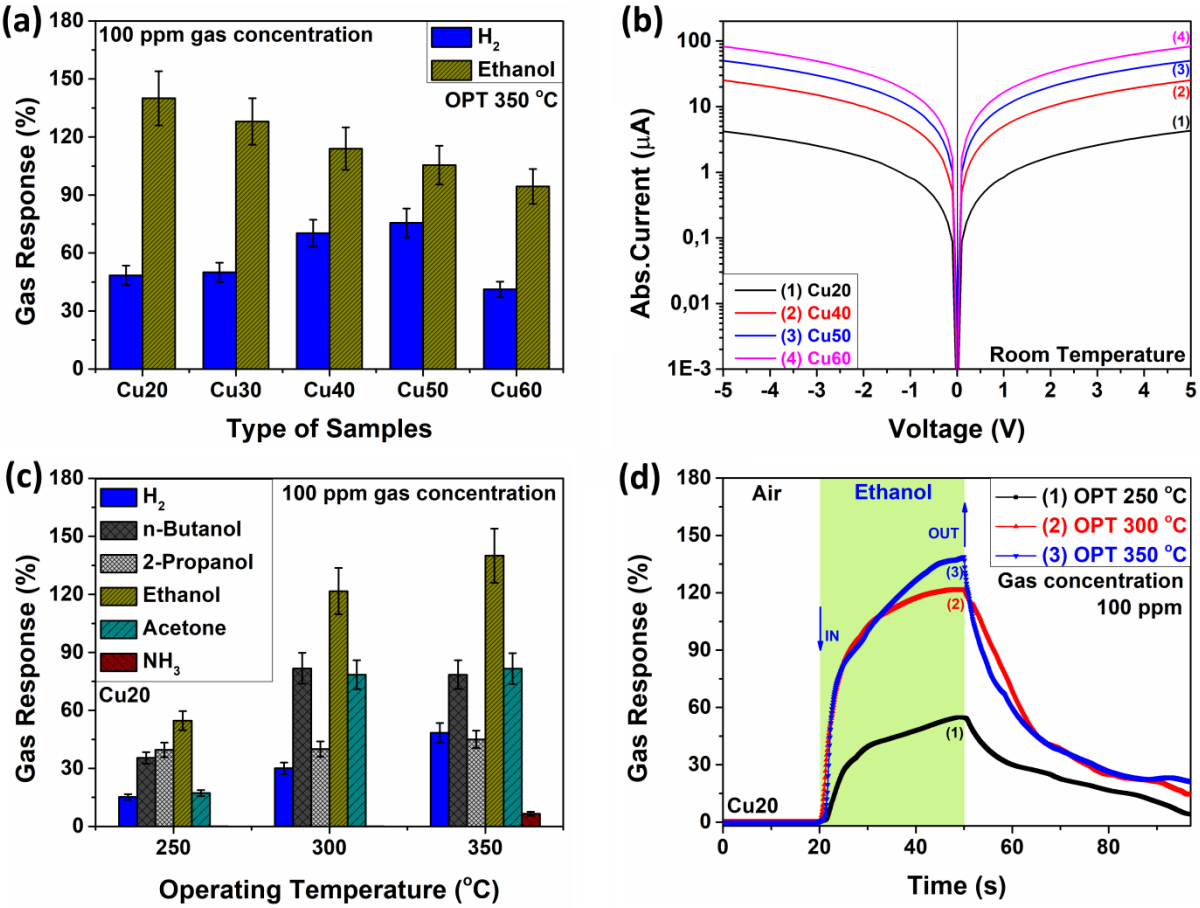

Figure 4. (a) Hydrogen and ethanol response of the CuO/Cu_2O samples with different thicknesses of 20 nm (Cu20), 30 nm (Cu30), 40 nm (Cu40), 50 nm (Cu50) and 60 nm (Cu60), respectively at the operating temperature of 350°C; (b) The *I-V* current-voltage characteristic of the CuO/Cu_2O Cu20, Cu4, Cu50 and Cu60 samples, measured at room temperature; (c) Response to different gases (hydrogen, *n*-butanol, 2-propanol, ethanol, acetone and ammonia) versus operating temperature of the CuO/Cu_2O Cu20 samples; (d) Dynamic response to ethanol of the CuO/Cu_2O Cu20 samples.

Cite this paper as : O. Lupan, D. Santos-Carballal, N. Ababii, N. Magariu, S. Hansen, A. Vahl, L. Zimoch, M. Hoppe, T. Pauporté, V. Galstyan, V. Sontea, L. Chow, N. H de Leeuw, F. Faupel, R. Adelung, E. Comini, $TiO_2/Cu_2O/CuO$ Multi-nanolayers as Sensors for H_2 and VOCs: An Experimental and Theoretical Investigation.
ACS Appl. Mater. Interfaces 13 (2021) 32363–32380.

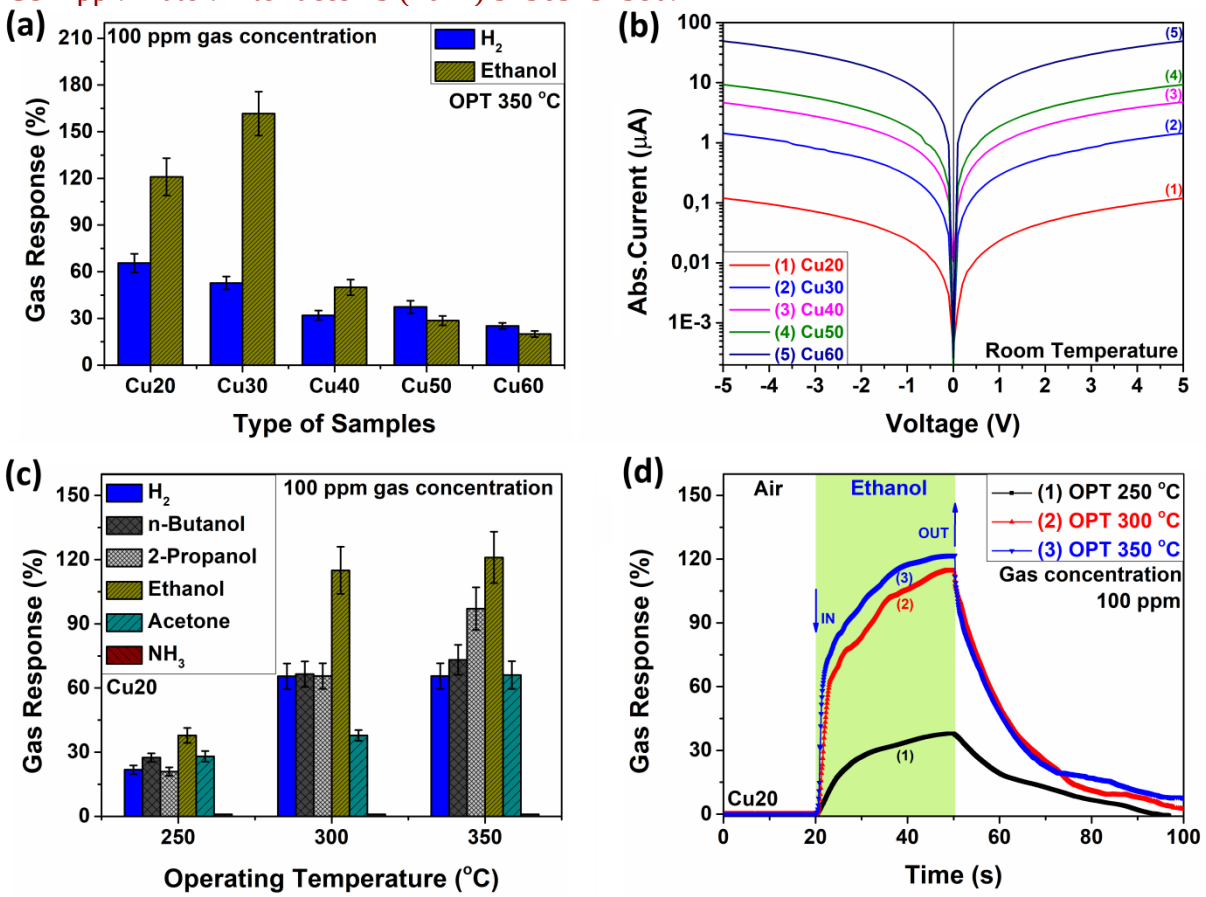

Figure 5. (a) Hydrogen and ethanol responses of the $TiO_2/CuO/Cu_2O$ samples with different thicknesses of 20 nm (Cu20), 30 nm (Cu30), 40 nm (Cu40), 50 nm (Cu50) and 60 nm (Cu60), respectively, measured at 350ºC; (b) The current-voltage characteristic at room temperature; (c) Response to different compounds (hydrogen, *n*-butanol, 2-propanol, ethanol, acetone and ammonia) versus operating temperature of the $TiO_2/CuO/Cu_2O$ Cu20 samples; (d) Dynamic response to ethanol of the $TiO_2/CuO/Cu_2O$ Cu20 samples.

Cite this paper as : O. Lupan, D. Santos-Carballal, N. Ababii, N. Magariu, S. Hansen, A. Vahl, L. Zimoch, M. Hoppe, T. Pauporté, V. Galstyan, V. Sontea, L. Chow, N. H de Leeuw, F. Faupel, R. Adelung, E. Comini, $TiO_2/Cu_2O/CuO$ Multi-nanolayers as Sensors for H_2 and VOCs: An Experimental and Theoretical Investigation.
ACS Appl. Mater. Interfaces 13 (2021) 32363–32380.

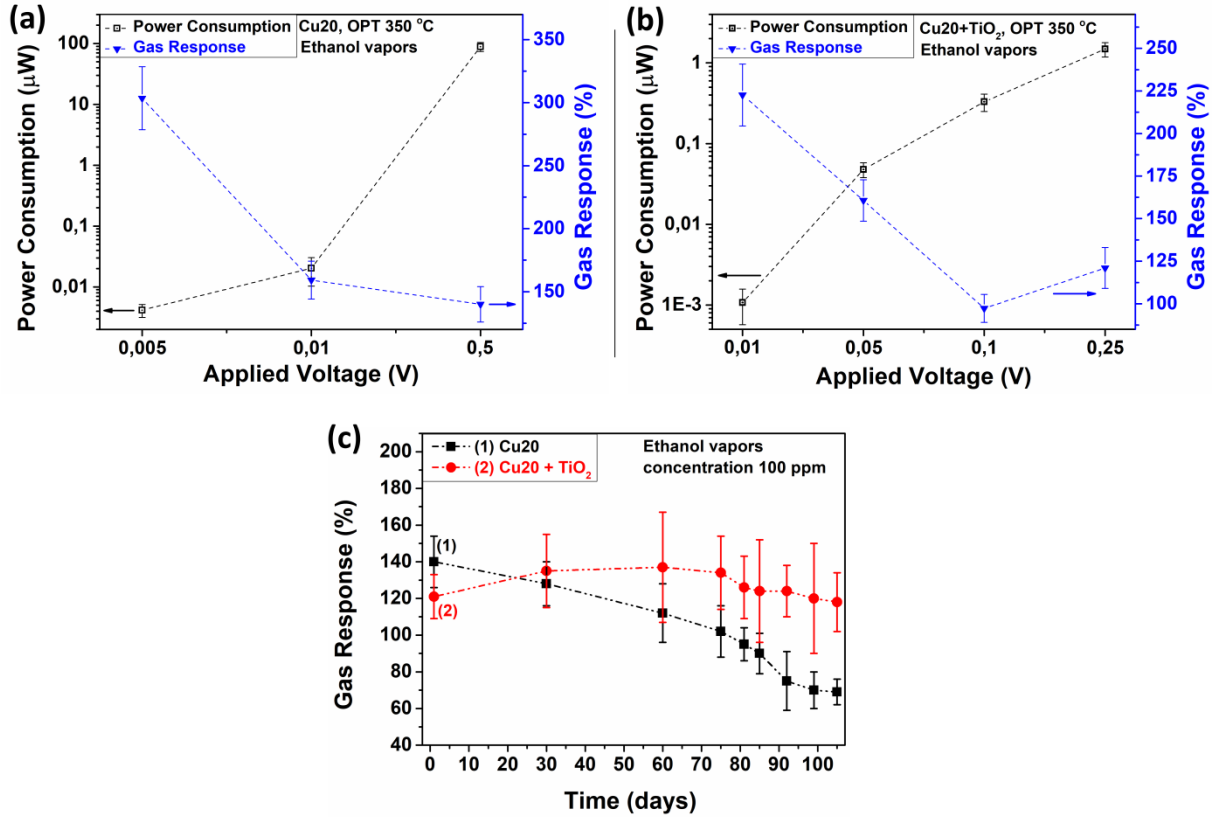

Figure 6. Dependence of the power consumption and the gas response with respect to the applied voltage for the (a) CuO/CuO_2 and (b) $TiO_2/CuO/CuO_2$ samples with thickness of 20 nm (Cu20); (c) Variation of gas response to ethanol vapors over time for the CuO/CuO_2 and $TiO_2/CuO/CuO_2$ samples with thickness of 20 nm (Cu20).

Cite this paper as : O. Lupan, D. Santos-Carballal, N. Ababii, N. Magariu, S. Hansen, A. Vahl, L. Zimoch, M. Hoppe, T. Pauporté, V. Galstyan, V. Sontea, L. Chow, N. H de Leeuw, F. Faupel, R. Adelung, E. Comini, $TiO_2/Cu_2O/CuO$ Multi-nanolayers as Sensors for H_2 and VOCs: An Experimental and Theoretical Investigation.
ACS Appl. Mater. Interfaces 13 (2021) 32363–32380.

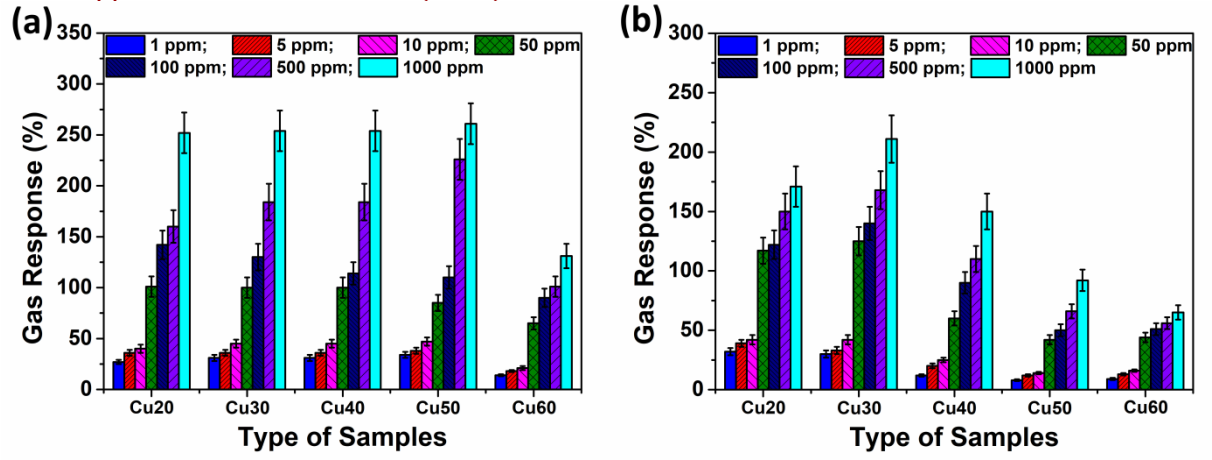

Figure 7. Gas response to various concentrations of ethanol vapor measured at 350 ^oC versus the type of samples for the (a) CuO/Cu_2O; and (b) $TiO_2/CuO/Cu_2O$ samples with different thicknesses of 20 nm (Cu20), 30 nm (Cu30), 40 nm (Cu40), 50 nm (Cu50) and 60 nm (Cu60).

Cite this paper as : O. Lupan, D. Santos-Carballal, N. Ababii, N. Magariu, S. Hansen, A. Vahl, L. Zimoch, M. Hoppe, T. Pauporté, V. Galstyan, V. Sontea, L. Chow, N. H de Leeuw, F. Faupel, R. Adelung, E. Comini, $TiO_2/Cu_2O/CuO$ Multi-nanolayers as Sensors for H_2 and VOCs: An Experimental and Theoretical Investigation.
ACS Appl. Mater. Interfaces 13 (2021) 32363–32380.

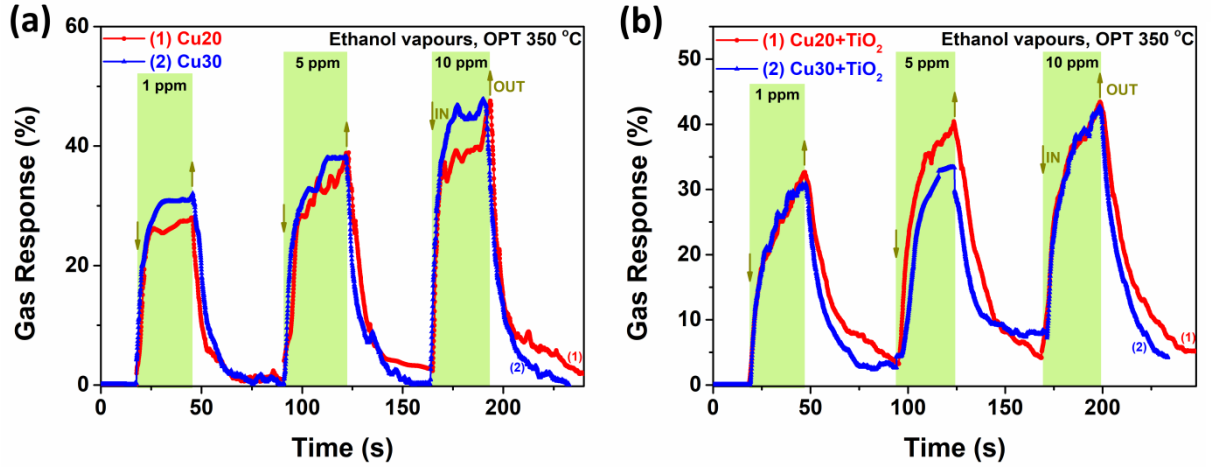

Figure 8. Dynamic response at 1, 5 and 10 ppm of ethanol vapor for the: (a) CuO/Cu_2O; and (b) $TiO_2/CuO/Cu_2O$ samples with various thicknesses of 20 nm (Cu20) and 30 nm (Cu30).

Cite this paper as : O. Lupan, D. Santos-Carballal, N. Ababii, N. Magariu, S. Hansen, A. Vahl, L. Zimoch, M. Hoppe, T. Pauporté, V. Galstyan, V. Sontea, L. Chow, N. H de Leeuw, F. Faupel, R. Adelung, E. Comini, $TiO_2/Cu_2O/CuO$ Multi-nanolayers as Sensors for H_2 and VOCs: An Experimental and Theoretical Investigation.
ACS Appl. Mater. Interfaces 13 (2021) 32363–32380.

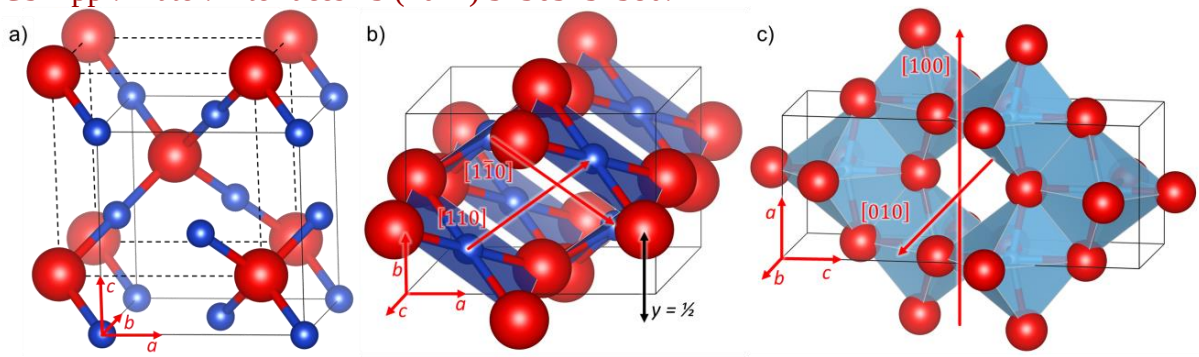

Figure 9. (a) Conventional cubic unit cell containing two formula units (f.u.) of cuprite Cu_2O. Solid lines represent the face-centred cubic (*fcc*) sublattice of Cu ions and dashed lines indicate the body-centred cubic (*bcc*) sublattice of O atoms. (b) Conventional monoclinic unit cell containing 4 f.u. of tenorite CuO. The $^{1}_{\infty}[CuO_{4/2}]$ chains are shown along the [110] and [1$\bar{1}$0] directions, while the ideal staggering parameter *y* is represented in direct coordinates. (c) Conventional tetragonal unit cell containing 4 f.u. of anatase TiO_2. The channels along the [100] and [010] directions are shown. Crystallographic directions are indicated for all structures. O atoms are in red, Cu atoms are in dark blue and Ti atoms are in light blue. Polyhedral representations are used for the square planar Co atoms and the distorted octahedral Ti atoms.

Cite this paper as : O. Lupan, D. Santos-Carballal, N. Ababii, N. Magariu, S. Hansen, A. Vahl, L. Zimoch, M. Hoppe, T. Pauporté, V. Galstyan, V. Sontea, L. Chow, N. H de Leeuw, F. Faupel, R. Adelung, E. Comini, $TiO_2/Cu_2O/CuO$ Multi-nanolayers as Sensors for H_2 and VOCs: An Experimental and Theoretical Investigation.
ACS Appl. Mater. Interfaces 13 (2021) 32363–32380.

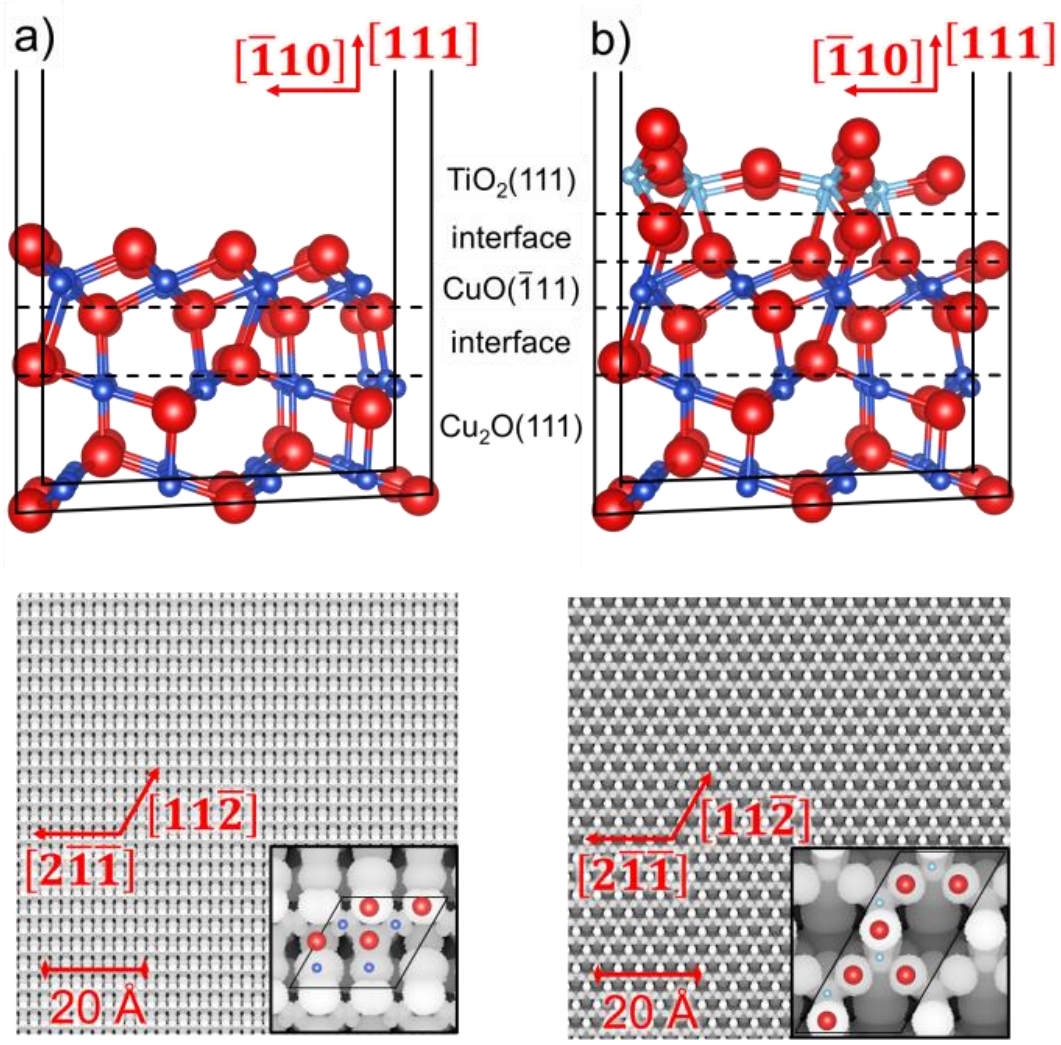

Figure 10. Top panels show the structure of the (a) binary CuO($\bar{1}$11)/Cu_2O(111) and (b) ternary TiO_2(111)/CuO ($\bar{1}$11) /Cu_2O(111) interfaces. Bottom panels display the simulated scanning tunnelling microscopy (STM) images using a bias of: (a) V = 1.0 eV; and (b) V = −0.5 eV, a density of (a) ρ = 0.0025 e Å^{-3}; and (b) ρ = 0.0010 e Å^{-3} as well as a tip distance of: (a) d = 1.21 Å; and (b) d = 1.62 Å. Crystallographic directions are indicated with respect to the Cu_2O(111) substrate. O atoms are in red, Cu atoms are in dark blue and Ti atoms are in light blue.

Cite this paper as : O. Lupan, D. Santos-Carballal, N. Ababii, N. Magariu, S. Hansen, A. Vahl, L. Zimoch, M. Hoppe, T. Pauporté, V. Galstyan, V. Sontea, L. Chow, N. H de Leeuw, F. Faupel, R. Adelung, E. Comini, $TiO_2/Cu_2O/CuO$ Multi-nanolayers as Sensors for H_2 and VOCs: An Experimental and Theoretical Investigation.
ACS Appl. Mater. Interfaces 13 (2021) 32363–32380.

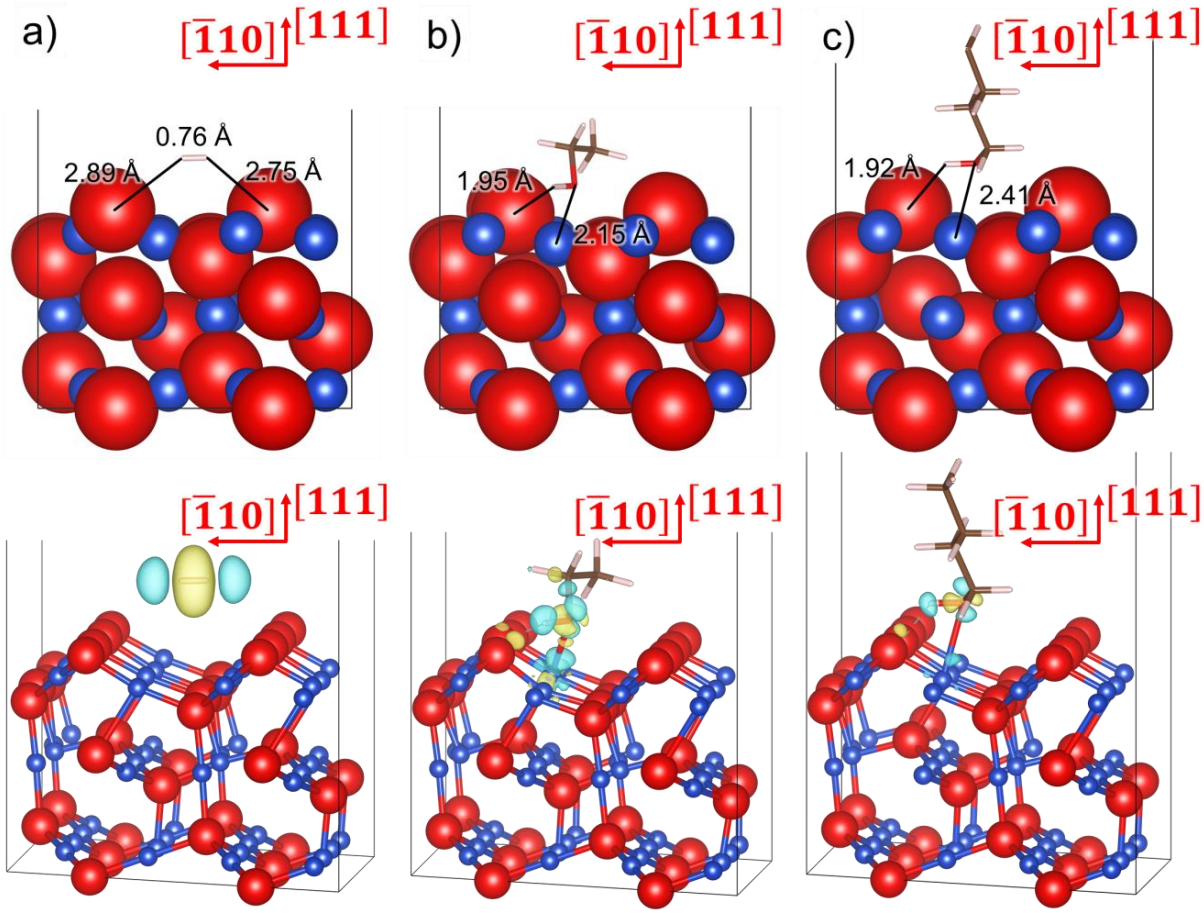

Figure 11. Adsorption of: (a) H_2, (b) C_2H_5OH and (c) *n*-C_4H_9OH on the $CuO(\bar{1}11)/Cu_2O(111)$ heterostructure. Interatomic distances are indicated in the top panels whilst the charge density flow ($\Delta\rho$) is represented in the bottom panels. Electron density gain and depletion regions are shown in yellow and green colours, respectively. Isosurfaces display a value of ±0.005 e $Å^{-3}$. Crystallographic directions are indicated with respect to the $Cu_2O(111)$ substrate. The binary heterostructures are displayed using the (top panels) space-filling and (bottom panels) ball-and-stick representation, whereas the adsorbates are shown using the stick representation. O atoms are in red, H atoms are in white, C atoms are in brown and Cu atoms are in dark blue.

Cite this paper as : O. Lupan, D. Santos-Carballal, N. Ababii, N. Magariu, S. Hansen, A. Vahl, L. Zimoch, M. Hoppe, T. Pauporté, V. Galstyan, V. Sontea, L. Chow, N. H de Leeuw, F. Faupel, R. Adelung, E. Comini, $TiO_2/Cu_2O/CuO$ Multi-nanolayers as Sensors for H_2 and VOCs: An Experimental and Theoretical Investigation.
ACS Appl. Mater. Interfaces 13 (2021) 32363–32380.

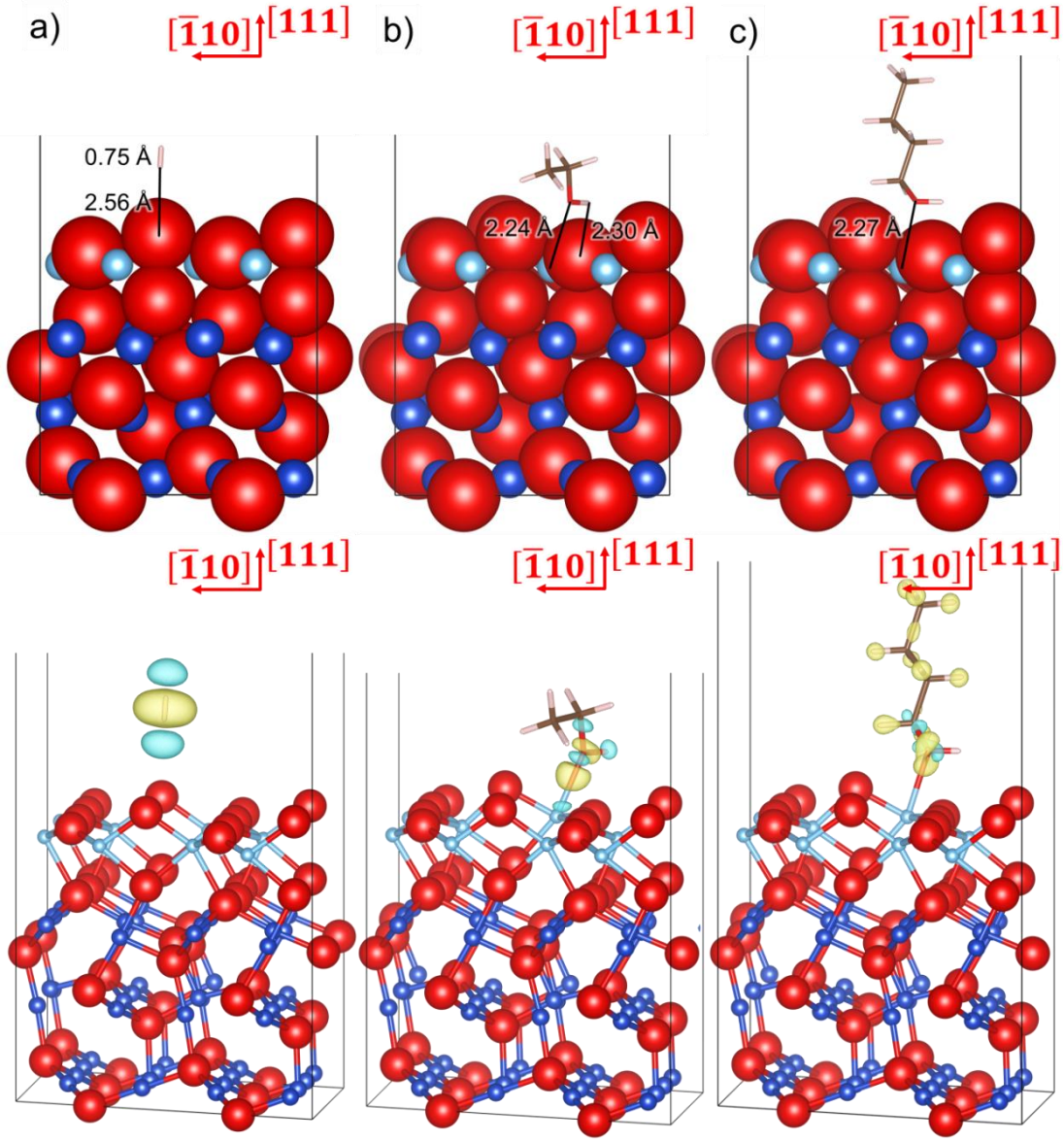

Figure 12. Adsorption of: (a) H_2, (b) C_2H_5OH and (c) *n*-C_4H_9OH on the $TiO_2(111)/CuO(\bar{1}11)/Cu_2O(111)$ heterostructure. Interatomic distances are indicated in the top panels whilst the charge density flow ($\Delta\rho$) is represented in the bottom panels. Electron density gain and depletion regions are shown in yellow and green colours, respectively. Isosurfaces display a value of ±0.005 e $Å^{-3}$. Crystallographic directions are indicated with respect to the $Cu_2O(111)$ substrate. The ternary heterostructures are displayed using the (top panels) space-filling and (bottom panels) ball-and-stick representation, whereas the adsorbates are shown using the stick

Cite this paper as : O. Lupan, D. Santos-Carballal, N. Ababii, N. Magariu, S. Hansen, A. Vahl, L. Zimoch, M. Hoppe, T. Pauporté, V. Galstyan, V. Sontea, L. Chow, N. H de Leeuw, F. Faupel, R. Adelung, E. Comini, $TiO_2/Cu_2O/CuO$ Multi-nanolayers as Sensors for H_2 and VOCs: An Experimental and Theoretical Investigation.
ACS Appl. Mater. Interfaces 13 (2021) 32363–32380.
representation. O atoms are in red, H atoms are in white, C atoms are in brown, Cu atoms are in

dark blue and Ti atoms are in light blue.

Table of Contents.